



# Antimicrobial and antibiofilm photodynamic therapy against vancomycin resistant *Staphylococcus aureus* (VRSA) induced infection in vitro and in vivo

Farheen Akhtar<sup>a</sup>, Asad U. Khan<sup>a,\*</sup>, Lama Misba<sup>a</sup>, Kafil Akhtar<sup>b</sup>, Asif Ali<sup>c</sup>

<sup>a</sup> Medical Microbiology and Molecular Biology Lab., Interdisciplinary Biotechnology Unit, Aligarh Muslim University, Aligarh, India

<sup>b</sup> Department of Pathology, JNMC, A.M.U., Aligarh, India

<sup>c</sup> Department of Biochemistry, F/o Medicine, JNMC A.M.U., Aligarh, India

## ARTICLE INFO

### Keywords:

Antimicrobial photodynamic therapy (aPDT)  
Antimicrobial resistance  
Preformed-biofilm  
Curcumin  
Blue laser light  
Vancomycin resistant *Staphylococcus aureus* (VRSA)  
Skin abrasion  
Rat model  
Cytokine profiling

## ABSTRACT

Biofilm mediated infection caused by multi-drug resistant bacteria are difficult to treat since it protects the microorganisms by host defense system, making them resistant to antibiotics and other antimicrobial agents. Combating such type of nosocomial infection, especially in immunocompromised patients, is an urgent need and foremost challenge faced by clinicians. Therefore, antimicrobial photodynamic therapy (aPDT) has been intensely pursued as an alternative therapy for bacterial infections. aPDT leads to the generation of reactive oxygen species (ROS) that destroy bacterial cells in the presence of a photosensitizer, visible light and oxygen. Here, we elucidated a possibility of its clinical application by reducing the treatment time and exposing curcumin to 20 J/cm<sup>2</sup> of blue laser light, which corresponds to only 52 s to counteract vancomycin resistant *Staphylococcus aureus* (VRSA) both in vitro and in vivo. To understand the mechanism of action, the generation of total reactive oxygen species (ROS) was quantified by 2',7'-dichlorofluorescein diacetate (DCFH-DA) and the type of phototoxicity was confirmed by fluorescence spectroscopic analysis. The data showed more production of singlet oxygen, indicating type-II phototoxicity. Different anti-biofilm assays (crystal violet and congo red assays) and microscopic studies were performed at sub-MIC concentration of curcumin followed by treatment with laser light against preformed biofilm of VRSA. The result showed significant reduction in the preformed biofilm formation. Finally, its therapeutic potential was validated in skin abrasion wistar rat model. The result showed significant inhibition of bacterial growth. Furthermore, immunomodulatory analysis with rat serum was performed. A significant reduction in expression of proinflammatory cytokines TNF- $\alpha$  and IL-6 were observed. Hence, we conclude that curcumin mediated aPDT with 20 J/cm<sup>2</sup> of blue laser treatment (for 52 s) could be used against multi-drug resistant bacterial infections and preformed biofilm formation as a potential therapeutic approach.

## 1. Introduction

The multidrug-resistant (MDR) bacterial infections have been considered as a global threat [1]. Colistin, a class of polypeptide, which is being used as 'last-line' of defense against MDR infections, has also been proved to be ineffective due to resistance emergence [2]. Due to this therapeutic failure, new strategies need to be developed to combat with these emerging infections [3]. Such infections are even tough to treat in case of biofilm formation, being protected by host defense system, which make them less susceptible to antimicrobial. In recent decades, the treatment of *Staphylococcus aureus* biofilm mediated

infections has become more difficult as the prevalence of multi-drug resistant continues to upsurge. These foremost challenges have motivated many researchers in the prevailing situation to develop alternative therapeutic options. Consequently, antimicrobial photodynamic therapy (aPDT) has been emerged as a promising alternative approach against bacterial infections [4]. It has been used successfully for curing several diseases like cancer [5], age related macular degeneration [6,7], rheumatoid arthritis [8], skin disease [9–11] and arteriosclerosis [12]. Apart from this, various studies have been published depicting the effectiveness of photodynamic therapy against Gram-negative bacteria, Gram-positive bacteria, viruses, fungi, and parasites [11,13–22]. The

\* Corresponding author at: Medical Microbiology and Molecular Biology Lab., Interdisciplinary Biotechnology Unit, Aligarh Muslim University, Aligarh 202002, UP, India.

E-mail address: [asadukhan72@gmail.com](mailto:asadukhan72@gmail.com) (A.U. Khan).

<https://doi.org/10.1016/j.ejpb.2021.01.012>

Received 10 July 2020; Received in revised form 22 December 2020; Accepted 20 January 2021

Available online 25 January 2021

0939-6411/© 2021 Elsevier B.V. All rights reserved.

concept of antimicrobial photodynamic therapy is quite upfront and holds a promising modality in the treatment of microorganisms. It is based on a simple concept of using light of visible wavelength range, causing rapid and complete killing of microorganisms by generating highly reactive oxygen species (ROS) after their sensitization with a nontoxic photoactive drug in the presence of oxygen [23].

A photoactive drug or a photosensitizer should have a strong absorption peak in range of 650 nm to 800 nm (red to near-infrared), spectral region. Moreover, an ideal photosensitizer should possess a significant triplet quantum yield leading to ample production of ROS upon irradiation by controlled light sources, such as lasers and light emitting diode (LED) [24–26].

The mechanism of action involved in antimicrobial photodynamic therapy is merely dependent upon the ability of a photosensitizer to generate ROS on light irradiation. The non-toxic photosensitizer absorbs photons of light of the appropriate wavelength to get excited. Once excited, photosensitizer gets converted from excited singlet state to a long lived excited triplet state through intersystem crossing which subsequently reacts with ground (triplet) state  $O_2$  in two different ways [27]. In type-I reaction, it transfer electron to substrate (eg. lipid, nucleic acid and proteins) which leads to the formation of free radicals like hydroxyl radicals ( $OH^\bullet$ ), hydrogen peroxide ( $H_2O_2$ ) and superoxide ( $O_2^{\bullet-}$ ). Whereas, in type-II reaction it involves transfer of energy to molecular oxygen which leads to the generation of singlet state oxygen [28]. Due to non-specific nature of the death caused by ROS, and shorter exposure time to the photosensitizer, the expression of protective factors involved in the development of resistance is slowed down, making it difficult for bacterial cells to acquire resistance against antimicrobial photodynamic therapy [3].

Among different types of photosensitizers (chlorothiazides, porphyrins, phenothiazines, sulfonamides, and tetracyclines) known, Curcumin is one of the commonly used natural photosensitizer [29–32]. It is a polyphenolic compound from the spice turmeric (*Curcuma longa* L.) and has been identified as an efficient photosensitizer for inactivation of a broad range of microorganisms. It shows antimicrobial, antioxidant, anti-inflammatory, antitumor and antifungal properties [33–38]. Furthermore, curcumin plays a significant role in the process of wound healing by down regulating the production of pro-inflammatory cytokines such as tumor necrosis factor- $\alpha$  (TNF $\alpha$ ) and interleukins (ILs); stimulating healing growth factors, increasing fibroblast numbers, antioxidant enzymes, granulation tissue formation, and collagen deposition; and accelerating neovascularization, re-epithelialization and wound closure [39–43]. The therapeutic potential of curcumin is further enhanced because of its ability to absorb blue light in the wavelength range 400–500 nm of the visible spectrum [44]. Therefore, in view of above background, we have initiated to investigate the efficacy of curcumin mediated antimicrobial photodynamic therapy, to inhibit multidrug resistant infection in vitro as well as in vivo using VRSA induced skin abrasion both in normal and immunocompromised wistar rats that have been rendered temporarily neutropenic by cyclophosphamide administration.

## 2. Materials and methods

### 2.1. Compliance with ethical standards

This research was conducted in accordance with institutional ethical standards. The study on animals was approved by the “Jawaharlal Nehru Medical College, AMU, Institutional Animal Ethics Committee”, registration no. 401/GO/Re/S/2001/CPCSEA. All applicable international, national, and/or institutional guidelines for the care and use of animals were followed.

### 2.2. Bacterial strain and isolate identification

Clinical sample was collected from the burn patient with a sterile

swab and cultured on brain heart infusion (BHI) broth (HIMEDIA LABS, MUMBAI, INDIA) for 24 h and incubated at 37 °C [45].

BD Phoenix<sup>TM-100</sup> automated microbiology system (Gram positive susceptibility card) was used for primary identification. The species level identification of isolate was performed by 16 s rDNA sequencing. The strain was identified as *Staphylococcus aureus*. The pure culture of isolate was cryopreserved at –80 °C in 70% glycerol.

### 2.3. Antimicrobial susceptibility testing

Antimicrobial susceptibility was determined by the standard disc diffusion method using Mueller Hinton (MH) agar plates (HIMEDIA LABS, MUMBAI, INDIA) as per the Clinical and Laboratory Standards Institute (CLSI, 2016) guidelines. These antibiotics discs (vancomycin, colistin, polymyxin, ceftazidime, amikacin, aztreonam) were used in this study. This test was performed only to determine the antibiotic susceptibility of the isolated strain that will be further used with curcumin

### 2.4. Determination of bacteriostatic (MIC) and bactericidal (MBC) concentrations

Curcumin (HIMEDIA LABS, MUMBAI, INDIA) was used as photosensitizer. The stock solution of curcumin (20 mg/ml) was prepared in DMSO and stored at 4 °C in the dark. The minimum inhibitory concentration (MIC) of curcumin against VRSA was determined by microdilution method as per Clinical and Laboratory Standards Institute (CLSI) guidelines [46]. Stock solution of curcumin was serially diluted with BHI media in 96 well microtiter plate. Bacterial cell density was estimated by spectrophotometry (Optical Density; OD 0.8 at 600 nm). Diluted overnight culture ( $10^8$  CFU/ml) was added in each well followed by irradiation of 20 J/cm<sup>2</sup> with 405 nm wavelength blue laser light. The treated cells were incubated for 24 h at 37 °C. MICs were determined as the lowest concentration that completely inhibits visible bacterial growth whereas, MBC were determined by sub-culturing the test dilution on MH agar plates.

### 2.5. Photosensitization and light source

Diode laser (Model No-MDL-III-405; CNI, China) was used for photosensitization.

The effective radiant exposure of the light source was calculated as follows [47]:

$$\text{Energy fluency} = \text{Power density} \times \text{Time}$$

Where, power density (PD) is  $PD = P \text{ (mW)}/\text{Area (cm}^2\text{)}$ , P is the output power of the light source (300 mW) and A is the irradiated area. In the present study the photodynamic treatment was carried out in a U-bottom microtiter plate. Therefore, samples acquire the shape of a hemisphere; hence the irradiated area was  $2\pi r^2$ , where r is the radius of the laser beam exposed, equal to 0.35 cm. The beam height from the base was 24.8 mm. The applied PD was 389.96 mW/cm<sup>2</sup> and the energy fluency was set to 20 J cm<sup>–2</sup> when irradiated for 52 s.

### 2.6. Detection of total ROS inside the cells

Endogenous ROS production after aPDT was quantified by fluorescence spectroscopy using 2', 7'- dichlorofluorescein-diacetate (DCFH-DA, SIGMA-ALDRICH, USA, CAS NUMBER: 4091-99-0). Overnight culture was centrifuged at 10,000g for 15 min. Pellets were washed twice with phosphate buffer saline at pH 7.4 and finally re-suspended in PBS by adjusting the cell density to  $10^8$  CFU/ml followed by incubation for 10 min with 10  $\mu$ M DCFH-DA. At the end of incubation, the cells were treated with sub-MIC concentration (78  $\mu$ g/ml) of curcumin and irradiated with 20 J/cm<sup>2</sup> of light dose corresponding to 52 s while the control (PBS) was left untreated. In only light treated group, we have irradiated cells with 20 J/cm<sup>2</sup> laser light without curcumin. Thereafter, the fluorescence intensity produced from DCFH-DA was measured by

excitation at 485 nm using slit width 1.5 nm [48].

## 2.7. Fluorescence probe experiments

Fluorescence probe (hydroxyphenyl fluorescein [HPF]) was used to determine the HO<sup>•</sup> produced by curcumin upon irradiation [49]. The bacterial suspension (10<sup>8</sup> CFU/ml) was incubated with HPF (final concentration of 10 µM) for 10 min in PBS. After incubation, the cells were treated with sub-MIC concentration of curcumin and irradiated with 20 J/cm<sup>2</sup> of light dose corresponding to 52 s in aPDT treated group while the control was left untreated. The fluorescence intensity was measured by excitation at 492 nm using slit width 1.5 nm [48].

## 2.8. Detection of singlet oxygen

9, 10-Anthracenediylbis (methylene) dimalonate acid (AMDA, SIGMA-ALDRICH, USA, CAS NUMBER: 307554-62-7) was used to quantify the <sup>1</sup>O<sub>2</sub> quantum yields of curcumin. 10 µM AMDA was added to solution containing VRSA (10<sup>8</sup> CFU/ml) in PBS followed by the treatment as explained above. The relative amount of <sup>1</sup>O<sub>2</sub> generated in each solution was determined by recording the decrease in the 399-nm absorption band of AMDA as a function of 405 nm of laser light irradiation. The 399-nm OD (optical density) decay is a measure of the amount of <sup>1</sup>O<sub>2</sub> generated [50].

## 2.9. In vitro estimation of VRSA load reduction by colony forming unit (CFU/ml)

The efficacy of curcumin mediated aPDT on the viability of vancomycin resistant *Staphylococcus aureus* preformed biofilm was investigated using following protocol. Overnight culture of VRSA was resuspended to a final concentration of 10<sup>8</sup> CFU/mL in fresh BHI supplemented with 1% sucrose. Aliquots (100 µl) of the diluted bacterial suspension were added in each well of 96 well microtitre plate and incubated for 24 h at 37 °C. Prior to the treatment, the remaining non-adherent bacteria were removed by washing with sterile PBS. Thereafter, preformed biofilm was incubated with sub-MIC concentration of curcumin in the dark for 30 min and then treated with 20 J/cm<sup>2</sup> energy density blue laser light. Control (matured biofilm in phosphate buffer saline without any treatment) was left untreated. Biofilm was then disrupted by vortexing followed by 10 fold serial dilution. 100 µl aliquots were plated onto BHI agar plate and incubated at 37 °C for 24 h. A number of grown colonies were then counted [51].

## 2.10. Quantification of biofilm formation by crystal violet assay

Biofilm formation by VRSA, after treatment with curcumin-aPDT (curcumin-antimicrobial photodynamic therapy), was evaluated using crystal violet assay. Preformed biofilm was grown for 24 h as described in bacterial load reduction (CFU/ml). Prior to the treatment, the exhausted media was removed from each well. Thereafter, the biofilm was incubated with sub-MIC concentration of curcumin for 30 mins followed by 20 J/cm<sup>2</sup> of irradiation, corresponding to 52 s in aPDT treated group. Control was left untreated. Subsequently, the control and treated biofilm-coated wells of microtiter plates were fixed with formalin (37%, diluted 1:10) and 2% sodium acetate. Biofilms in all the wells were subsequently stained using 200 µl of 0.1% crystal violet for 15 min at room temperature. After two rinses with sterile PBS, unbound dye was removed from the cells with 100 µl of 95% ethanol. The plates were shaken for 10 min to allow full release of the dye and the absorbance was recorded by measuring optical density of suspension at 630 nm by microplate reader (BIORAD MICROPLATE READER, INDIA) [48]. The amount of EPS produced was estimated using the following formula described by López-Moreno et al., 2014 [52].

OD of blank CR-OD of the supernatant = OD of bound CR (EPS produced)

## 2.11. Estimation of exopolysaccharide production

The Congo red (CR)-binding assay was used to estimate the production of exopolysaccharide (EPS), as reported earlier [53]. Same photodynamic treatment was given on preformed biofilm as described above. After treatment exhausted media were removed and wells were washed twice with PBS. 100 µl of fresh media and 50 µl of CR (0.5 mM) were then added to each wells containing control and treated samples. 100 µl of medium along with 50 µl CR was also used for blank measurements (blank CR). Thereafter, the microtiter plate was incubated for 2 h at 37 °C. After incubation, the contents of each wells was transferred to micro-centrifuge tubes followed by centrifugation at 10,000g for 5 min. The supernatants were transferred to fresh microtiter plate and colorimetric change was measured using microtiter plate reader (BIO-RAD iMark TM Microplate reader) at 490 nm [18].

## 2.12. Confocal laser scanning microscopy (CLSM)

Confocal laser scanning microscopy (CLSM) was performed to analyze the consequence of curcumin mediated antimicrobial photodynamic therapy on VRSA biofilm after irradiation with 20 J/cm<sup>2</sup> of light dose. Biofilm was grown in covered glass bottom confocal dishes (GENETIX BIOTECH ASIA PVT. LTD., NEW DELHI, INDIA) for 24 h at 37 °C. After incubation, sterile PBS was used to wash the confocal dishes to remove the loosely bound cells. The adhered cells or the preformed biofilm was treated as describe above, while controls were left untreated. Thereafter, the biofilm was then stained with propidium iodide (PI) and syto9 followed by incubation at 37 °C for 1 h. Fluorescence emission was observed using Fluo View FV1000 (OLYMPUS, TOKYO, JAPAN) confocal laser scanning microscope equipped with argon and HeNe laser with an excitation wavelength of 536 and 488 nm, respectively [48].

## 2.13. Scanning electron microscopy (SEM)

SEM (Scanning electron microscopy) was performed to analyze the morphology of preformed biofilm treated with curcumin-aPDT. The preformed biofilm was allowed to grown upon a glass coverslip in 6 well plate and treated as describe above. After treatment, biofilms in each sample (Control and treated) were fixed with 2% formaldehyde + 2.5% glutaraldehyde in PBS for 2 h at 4 °C. Different concentrations of ethanol (20%, 40%, 60%, 80%, and 100%) were used to dehydrate the fixed samples. The coverslips were dried, mounted and sputter coated with gold–palladium and analyzed under scanning electron microscope [48].

## 2.14. Cytotoxicity assay

A cytotoxicity assay was performed on human monocytic cell line THP1. The THP1 was cultured in ROSWELL PARK MEMORIAL INSTITUTE (RPMI) 1640, supplemented with 10% fetal bovine serum (FBS) and 1% antibiotic i.e. penicillin–streptomycin (pen-strep) at 37 °C, and 95% humidified incubator with 5% CO<sub>2</sub>. Sterile conditions were maintained all the times. Cells (~10<sup>5</sup> cells/well) were seeded in 96-well plates, left overnight to adhere (THP1 as a monocyte were differentiated into macrophages using PMA of stock solution 10 ng per µl and working solution of 20 ng per ml) cells were exposed to and then treated with various concentrations of curcumin (39 µg/ml, 78 µg/ml and 400 µg/ml) in the presence as well as in the absence of laser irradiation. After 24 h, cell survival was determined by a standard 3-(4,5-dimethyl thiazol-2-yl)-2,5-diphenyl tetrazolium bromide (MTT) assay. The supernatants were removed and 90 µl of fresh medium and 10 µl of MTT (1 mg/ml) solution were added to each well, followed by incubation for 4 h at 37 °C. The formazan crystals formed by the reduction of MTT were dissolved in 150 µl of DMSO and the absorbance was quantified by measuring its optical density at a wavelength of 570 nm using spectrophotometer [54].

## 2.15. Antimicrobial photodynamic therapy against VRSA induced topical infection in male wistar rats

### 2.15.1. Rat model of skin abrasion

In the experiment, a total of 40 adult male wistar rats, weighing, 250–300 g, were used. The rats were divided into 2 main groups i.e. the normal group and the immunocompromised group. Each group consisted of 20 rats, which were further sub-divided into 4 groups of 5 rats each. Group 1 consisted of rats without infection (Control); Group 2 contained rats with infection (Untreated); Group 3 contained rats treated with only curcumin (78 µg/ml); Group 4 was rats treated with curcumin (78 µg/ml) + laser light (20 J/cm<sup>2</sup>);

The animals were housed 5 per cage and kept on a 12-hour light/dark cycle with access food and water ad libitum. At day 1 and 4, rats were administered two doses of cyclophosphamide. The first dose was 150 mg cyclophosphamide per kg of rat body weight (150 mg/kg), injected intraperitoneally (i.p.) followed by the second dose of 100 mg/kg. This treatment reduced peripheral blood neutrophils to < 100/ml blood [45], fostering a more susceptible environment for infection in the rats. Before the creation of wounds, rats were anesthetized with i.p. injections of ketamine/xylazine cocktail and then shaved on the dorsal surfaces using 28-gauge needles. Skin abrasion wounds were made by creating 6 × 6 crossed scratch lines within a defined 1 × 1 cm<sup>2</sup> area [2,45].

### 2.15.2. Infection induction

Five minutes after wounding, an aliquot of 50 µl suspension containing 10<sup>8</sup> CFU of VRSA in PBS was inoculated over each defined area in normal and immunocompromised rats containing the crossed scratches with a pipette tip. They were observed carefully for symptoms of disease (weight, ruffled fur and inactivity) and rats that become moribund were sacrificed [55].

### 2.15.3. Antimicrobial photodynamic therapy on vancomycin resistant *Staphylococcus aureus* (VRSA) infected wistar rats

All experiments using rats that had been treated with curcumin were carried out under subdued room lighting or in the dark, except when illumination was taking place. Curcumin was added at sub-MIC concentration (78 µg/ml) in the middle and spread over the whole infected area. Thirty minutes after the addition of curcumin, irradiation was carried out with 405 nm of laser light for 52 s which corresponds to 20 J/cm<sup>2</sup> [45].

### 2.15.4. Effects of aPDT on the number of viable bacteria in the skin abrasion

In order to confirm the absence of VRSA colonization in the skin abrasion, bacterial load was measured for every sample by CFU counting on BHI agar plates and expressed as CFU per ml. Swab samples were taken from the infected skin surfaces of the rats after 24 h of the infection. Treatment was given after every 24 h for three weeks and then the samples from control and treated groups were serially diluted and plated on BHI agar plates for total cell counts. The plates were incubated at 37 °C for 24 h before enumeration of colonies of VRSA [56].

## 2.16. Histopathological analysis

Fresh skin biopsies of both control and aPDT treated rat groups were incised and fixed in 10% phosphate buffered formalin (pH 7.4). The tissues were then dehydrated in ascending grades of ethyl alcohol, cleared in xylene and mounted in molten paraplast at 58–62 °C. Serial 5-µm histological sections were cut and stained with haematoxylin and eosin (H/E) to examine microorganism response [57].

## 2.17. Effects of curcumin mediated aPDT on inflammatory markers

To determine the production level of cytokines, blood samples were

drawn and collected into sterile blood collection tubes from the eyes of controls, untreated, only curcumin treated and curcumin with light treated groups of normal and immunocompromised rats under anesthesia. Thereafter, all rats were immediately sacrificed as per the guidelines. The blood samples were centrifuged at 5000 rpm for 5 min. After centrifugation, the serum supernatant was aliquoted in micro-centrifuge tubes and stored at –80 °C for further analysis [58]. The commercially available enzyme-linked immunosorbent assay (ELISA) kits were used according to the manufacturers' protocol: Rat TNFα ELISA Kit (RAY BIOTECH, CAT: ELR-TNFA), Rat IL-6 ELISA Kit (RAY BIOTECH, CAT: ELR-IL6). The levels of TNF-α and IL-6 were measured by ELISA reader (BIORAD MICROPLATE READER, INDIA).

## 2.18. Statistical analysis

All data were presented as averages of the values obtained ± S.D. of three independent experiments. Test groups were compared with the control group using the Student's *t*-test. Free online software, one-way analysis of variance (ANOVA) [59] was used for the comparison of multiple means. For in vivo experiments, all the results were expressed as mean ± S.D. for five rats in each group. Data with  $P \leq \alpha = 0.05$  and  $P < \alpha = 0.01$  were considered to be statistically significant (following the confidence level of 95%).

## 3. Results

### 3.1. Antimicrobial susceptibility

The isolated strain of *Staphylococcus aureus* was found to be highly resistant against vancomycin (Supplementary figure S1).

### 3.2. Bacteria susceptibility assay

The MIC and MBC of curcumin in the presence as well as in the absence of laser irradiation against VRSA is shown in Table 1. The MIC value of curcumin-aPDT for VRSA was found to be 156.25 µg/ml whereas sub-MIC (1/2 of MIC) was found to be 78 µg/ml. Sub-minimum inhibitory concentration (sub-MIC) of curcumin (78 µg/ml = 1/2 of MIC) was taken as a standard to evaluate the antimicrobial and anti-biofilm effect of curcumin mediated photodynamic therapy against vancomycin resistant *Staphylococcus aureus* (VRSA).

### 3.3. Enhanced production of intracellular ROS

The result showed 4.8fold increase in DCF fluorescence intensity in only curcumin treated group. While 5.8 fold increase in the DCF fluorescence was observed when the cells were treated with curcumin followed by laser irradiation at a concentration of 78 µg/ml as compared to control group. This data clearly proved that more ROS were produced in curcumin-aPDT treated group than curcumin alone. Whereas, no ROS production was seen in the group treated with light only. Hence, for

**Table 1**

Determination of minimum inhibitory concentration (MIC) and minimum bactericidal concentration (MBC) concentration of curcumin against Vancomycin resistant *Staphylococcus aureus* (VRSA).

Strain : Vancomycin resistant <i>Staphylococcus aureus</i> (VRSA)				
S. No.	Treatment	Minimum inhibitory concentration (MIC) in µg/ml	Sub-MIC (1/2 of MIC) in µg/ml	Minimum bactericidal concentration (MBC) in µg/ml
1.	Only Curcumin	5000	2500	>5000
2.	Curcumin + light (20 J/cm <sup>2</sup> = 52 s)	156.25	78	312.5



further study, only curcumin and curcumin with light treated groups were selected (Fig. 1).

### 3.4. Quenching of hydroxyl radical

HPF probe was used to determine  $\cdot\text{OH}$  radicals formed by curcumin mediated aPDT in order to check if type I ROS generated. This data revealed that curcumin-aPDT caused quenching of  $\cdot\text{OH}$  radicals (Fig. 2A). It is evident from the results that more quenching of hydroxyl radical was observed in curcumin without light as compared to curcumin with light treatment. Since, laser treatment reduces the quenching effect of curcumin, therefore same concentration of curcumin with light shows less quenching as compared to curcumin without light.

### 3.5. Elevated production of singlet oxygen

The  $^1\text{O}_2$  production abilities of curcumin were also quantified in PBS by measuring the degradation rate of AMDA. Enhanced  $^1\text{O}_2$  quantum yield was observed at sub-MIC of curcumin followed by light irradiation as compared to only curcumin treated group (Fig. 2B). Since, the amount of ROS produced is directly proportional to the bacterial cell death; curcumin without light treated group shows less  $^1\text{O}_2$  production than curcumin with light irradiation. This confirmed that type II photochemistry is the major photochemical reaction involved in curcumin mediated aPDT.

### 3.6. Bacterial load reduction (CFU/ml)

A significant  $3.05 \log_{10}$  reduction in bacterial load was observed when preformed biofilm of VRSA was exposed to curcumin at sub-MIC ( $78 \mu\text{g/ml}$ ) concentration and subsequently to  $20 \text{ J/cm}^2$  of laser irradiation, which corresponds to 52 s. Whereas only  $1.19 \log_{10}$  reduction was found in the group treated with only curcumin (Fig. 3).

### 3.7. Reduction of VRSA biofilm when treated with curcumin mediated aPDT

The effect of curcumin mediated aPDT on preformed biofilm of VRSA is shown in Fig. 4A. A 37.32% of biofilm reduction was observed in only curcumin ( $78 \mu\text{g/ml}$ ) treated group while, approximately, 67.73% reduction in biofilm was found in curcumin with light treated group, as compared to control.

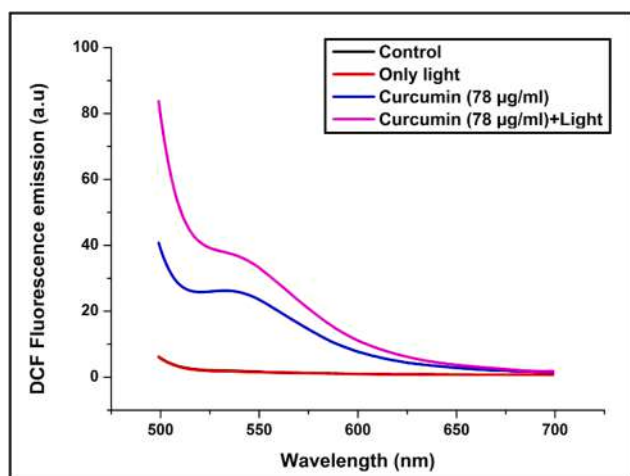


Fig. 1. Detection of total reactive oxygen species in VRSA by fluorescence intensity of 2',7'-dichlorofluorescein (DCF) after curcumin mediated aPDT with  $20 \text{ J/cm}^2$  of light irradiation. Control represents without any treatment.

### 3.8. Decrease level of EPS upon curcumin mediated aPDT

EPS formation is essential for the structure of biofilm, its spread and maintenance. The level of EPS was estimated by congo-red binding assay, which directly measures the relative amount of EPS after aPDT. A significant decrease in EPS level was detected in VRSA in the presence of curcumin followed by light irradiation (Fig. 4B). 47.94% EPS reduction was observed with sub-MIC ( $78 \mu\text{g/ml}$ ) concentration of curcumin with light, whereas 13.66% reduction was found in only curcumin treated group. The highest EPS level was seen in the control group without any treatment.

### 3.9. Impairment of biofilm architecture visualized through confocal microscopy

CLSM analysis was performed to check the consequence of aPDT on the viability of VRSA biofilm. In control group, lawn of green fluorescing VRSA cells were shown, indicating all live cells (Fig. 5A). Cells treated with only curcumin, showed both green (live) and red (dead) fluorescence as shown in Fig. 5B. However, most prominent reduction was seen in aPDT treated group. Majority of the cells were dead throughout the biofilm at  $78 \mu\text{g/ml}$  of concentration of curcumin with  $20 \text{ J/cm}^2$  of blue laser light treatment as shown in Fig. 5C.

### 3.10. SEM analysis of VRSA biofilm architecture

SEM analysis was carried out to elucidate the overall morphology of the cells in the biofilm after aPDT. Cells in the control group (Fig. 5D) were embedded in an EPS matrix that accelerates cell clustering. Remarkable reduction was found in the number of adherent bacteria upon treatment of biofilm with  $78 \mu\text{g/ml}$  (Fig. 5F) concentration of curcumin along with light irradiation, as compared to only curcumin treated (Fig. 5E) group. Furthermore, cells in aPDT treated groups were completely ruptured, became irregularly shaped and showed leakage of cellular constituents (Fig. 5F, enlarged image of curcumin + light treated VRSA biofilm is provided in the [supplementary information; figure S4](#)).

### 3.11. Cytotoxicity of curcumin mediated aPDT on human monocytic cell line THP1

The cytotoxic effect of curcumin mediated aPDT was evaluated by MTT assay. The relative cellular viability of human monocytic cell line THP1 in the presence of different concentrations ( $39 \mu\text{g/ml}$ ,  $78 \mu\text{g/ml}$  and  $400 \mu\text{g/ml}$ ) of curcumin with and without light irradiation is shown in Fig. 6. Almost 52% viability was observed at a concentration of  $400 \mu\text{g/ml}$  as compared to that used in this study. Thus, the test concentration of curcumin ( $78 \mu\text{g/ml}$ ) with light treatment ( $20 \text{ J/cm}^2 = 52 \text{ s}$ ) was found nontoxic to THP1 cell line.

### 3.12. In vivo experiments

#### 3.12.1. Curcumin mediated anti-microbial photodynamic therapy reduces bacterial load in normal and immunocompromised rat model of VRSA skin infection

Bacterial load was measured by CFU counting on BHI agar plates (Supplementary figure S3). The weekly recovery of rats over 3 weeks post treatment is shown in Fig. 7. The effects of photosensitization of curcumin demonstrated significant reduction in the bio-burden of VRSA in immunocompromised rats, which would otherwise develop severe infections. Curcumin-aPDT treated groups showed complete eradication of VRSA as compared to infection control group (Fig. 8). After 24 h of infection in immunocompromised rats, we found  $2.7 \log_{10}$  and  $4 \log_{10}$  reduction in only curcumin and curcumin with light treated groups, respectively, as compared to its untreated group. While in normal rats, we found  $2.2 \log_{10}$  and  $3.8 \log_{10}$  reduction in only curcumin and

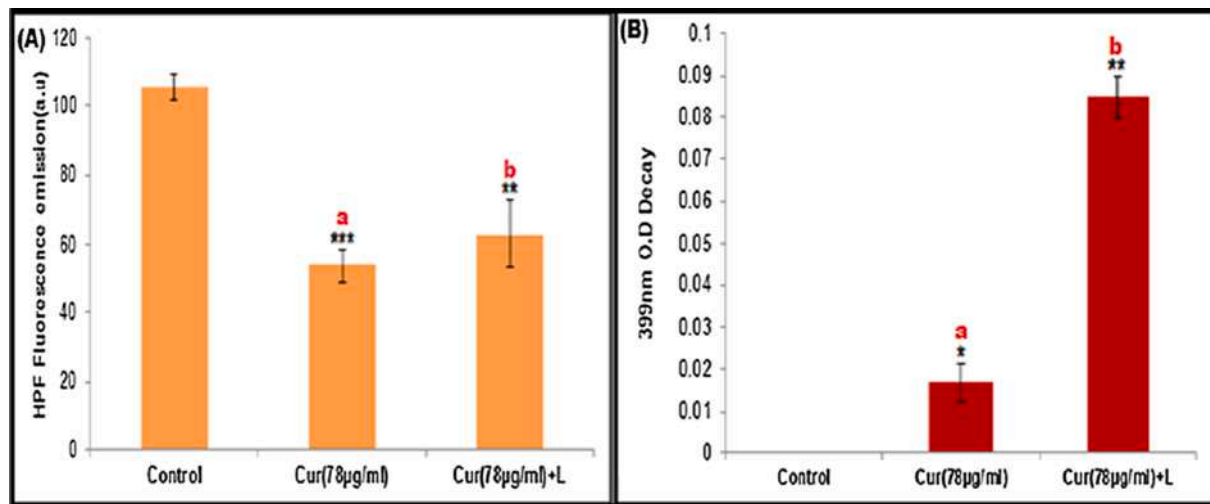


**Fig. 2.** Mechanism of aPDT: (A) Detection of  $\cdot\text{OH}$  radical (Type I) after  $20 \text{ J/cm}^2$  light irradiation by HPF fluorescence probe. (B) Quantification of singlet oxygen (Type II) by AMDA under  $20 \text{ J/cm}^2$  of light irradiation. Data are presented as mean  $\pm$  SD ( $n = 3$ ). Test groups were compared with the control group using the Student's  $t$ -test and one-way analysis of variance (ANOVA) was used for the comparison of multiple means. Data with  $p$ -value of  $<0.05$  (\* $p < 0.01$ , \*\* $p < 0.001$ , \*\*\* $p < 0.0001$ ) was considered statistically significant. a - Only curcumin treated group compared with control or untreated group; b - Curcumin + light treated group compared with control or untreated group.

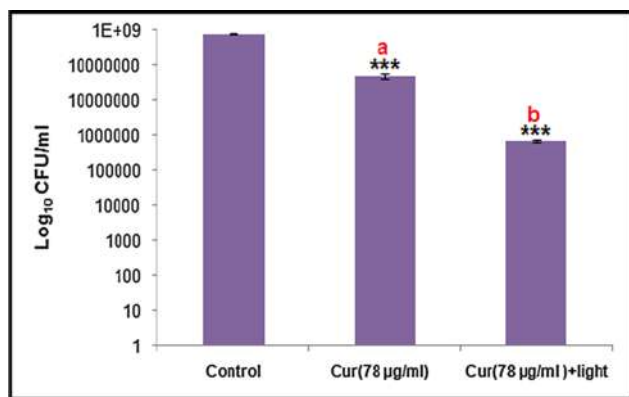


**Fig. 3.** Effect of aPDT on preformed vancomycin resistant *Staphylococcus aureus* (VRSA) biofilm: Preformed biofilm of VRSA was incubated with curcumin (78 µg/ml) followed by exposure to  $20 \text{ J/cm}^2$  of light. Control represent without curcumin and light treatment. Data are presented as mean  $\pm$  SD ( $n = 3$ ). Test groups were compared with the control group using the Student's  $t$ -test and one-way analysis of variance (ANOVA) was used for the comparison of multiple means. Data with  $p$ -value of  $<0.05$  (\* $p < 0.01$ , \*\* $p < 0.001$ , \*\*\* $p < 0.0001$ ) was considered statistically significant. a - Only curcumin treated group compared with control or untreated group; b - Curcumin + light treated group compared with control or untreated group.

curcumin with light treated group, respectively. In immunocompromised rats, reduction in bacterial counts after three weeks was found to be  $3.2 \log_{10}$  in only curcumin treated group. Whereas, in curcumin with light treated group almost complete eradication of bacterial load was observed. Curcumin with light treated group in normal rats showed complete recovery of skin abrasion as compared to its untreated group, which may be due to its innate immunity.

### 3.12.2. Histopathological observations

An expert pathologist did histopathological evaluations of the biopsy samples of rat skin. Haematoxylin and eosin stained sections of normal untreated rats showed the prevalence of focal lesions in the dermis with dense neutrophilic infiltrate. Acute inflammatory cells were dispersed around skin adnexa whereas immunocompromised untreated rats exhibited focally atrophied epidermis and hyperkeratosis with focal,

dense neutrophilic infiltrate in the epidermis and dermis extending to the deeper muscle fibres. Curcumin-aPDT treated normal rats showed atrophied stratified squamous epithelial cell with hyperkeratosis and sparsely dispersed neutrophilic infiltrate in the dermis. Focal atrophied ducts were also seen in the dermis while in immunocompromised rats, focally acanthotic stratified squamous epithelial cells with mild neutrophilic infiltrate in the papillary dermis and sparsely distributed inflammatory cells around the sebaceous glands were observed. In other treated sample (those which were treated with only curcumin), a moderate neutrophilic infiltrate was observed throughout epidermal, dermal and papillary dermal layers (Fig. 9).

### 3.12.3. Anti-inflammatory activity of curcumin followed by exposure of blue laser light in a rat model of skin abrasion

After the rats were sacrificed, two types of pro-inflammatory cytokines tumor necrosis factor- $\alpha$  (TNF- $\alpha$ ) and interleukin-6 (IL-6) were measured in the serum sample to evaluate the degree of inflammation. It was found that skin abrasion infected with VRSA, in both normal and immunocompromised rats has led to a significant increase in TNF- $\alpha$  and IL-6 levels ( $p < 0.05$ ). However, decreased levels of cytokines were produced in normal rat groups after infection as compared to immunocompromised group implying suppression of immune activities by cyclophosphamide.

In immunocompromised rats, the effective treatment dose of curcumin alone leads to substantial decrease in the production levels of these pro-inflammatory cytokines when compared with untreated group. However, remarkable decrease in IL-6 and TNF- $\alpha$  level was found in curcumin-aPDT treated group. The level of cytokines in normal rats was also found to be reduced after curcumin-aPDT treatment (Fig. 10). The obtained result showed that sub-MIC (78 µg/ml) concentration of curcumin on exposure to  $20 \text{ J/cm}^2$  of blue laser light restores immunosuppression and surges immunity by augmenting the productions of cytokines.

## 4. Discussion

The growing resistance in pathogenic bacteria against existing antibiotic remains a major concern for public health. *Staphylococcus aureus* infections represent a growing proportion of severe community-acquired and nosocomial infections [60–63]. Majority of these infections are now being caused by multidrug-resistant strains, including

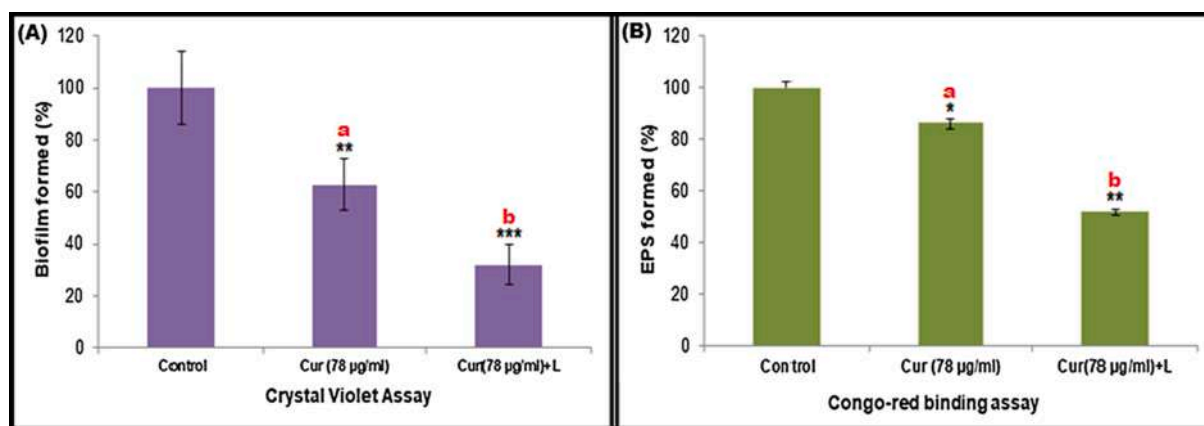


**Fig. 4.** (A) Inhibitory effect of curcumin mediated aPDT on preformed biofilm of VRSA quantified by Crystal violet assay. Absorbance was measured at 630 nm. (B) Congo-red assay: effect of curcumin mediated aPDT on extracellular polysaccharide substance (EPS) reduction. Absorbance was measured at 490 nm. Data are presented as mean  $\pm$  SD ( $n = 3$ ). Test groups were compared with the control group using the Student's  $t$ -test and one-way analysis of variance (ANOVA) was used for the comparison of multiple means. Data with  $p$ -value of  $<0.05$  (\* $p < 0.01$ , \*\* $p < 0.001$ , \*\*\* $p < 0.0001$ ) was considered statistically significant. a - Only curcumin treated group compared with control or untreated group; b - Curcumin + light treated group compared with control or untreated group.

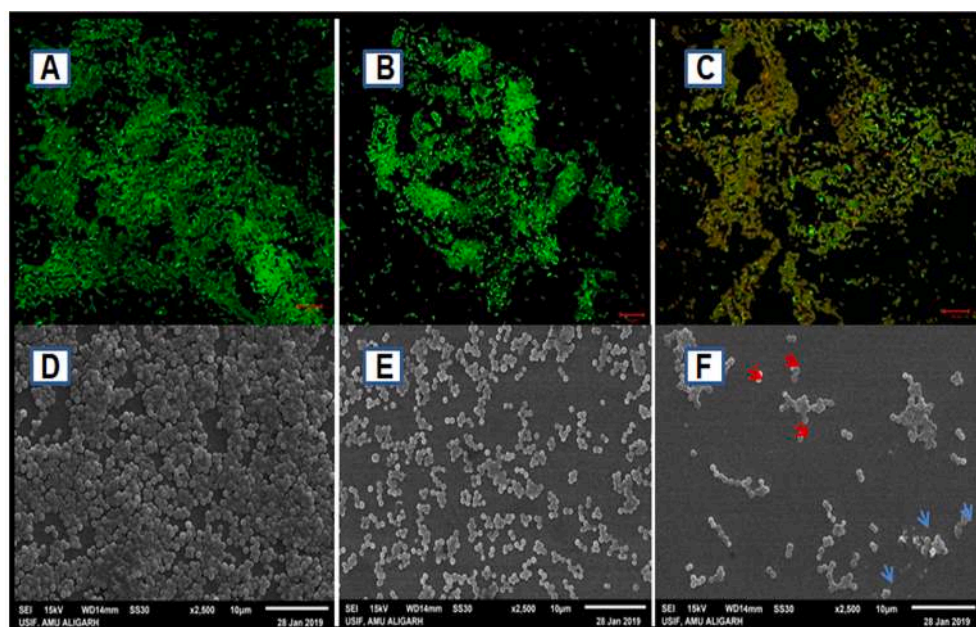


**Fig. 5.** Live/dead fluorescent staining images of VRSA biofilm: (A) Control biofilm, (B) Only curcumin (78 µg/ml) (C) Curcumin (78 µg/ml) + light. The images represent bacterial biofilm cells stained with SYTO 9 (green/live) and PI (red/dead). Scale bar = 10 µm. **Biofilm Assessment and Structural Imaging:** Scanning electron microscopy (SEM) images of VRSA biofilm. (D) Control biofilm, (E) Only curcumin (78 µg/ml) (F) Curcumin (78 µg/ml) + Light. Red arrow indicates bursting and release of cellular constituents while blue arrow indicates complete rupturing of the cells. (For interpretation of the references to colour in this figure legend, the reader is referred to the web version of this article.)

vancomycin or methicillin resistant *S. aureus* [64–67]. In such situation, when no antibiotic is left to treat, antimicrobial photodynamic therapy can be used as an alternative approach. When compared with other antimicrobial therapies, aPDT has several advantages such as absence of long-term toxicity, ability to kill microorganisms in a very less time and high repeatability without developing resistance [23,68]. Several studies have been reported depicting the efficacy of antimicrobial photodynamic therapy with various photosensitizers against *S. aureus* [69–71]. In the present study; we have examined the antimicrobial effect of curcumin-mediated aPDT against preformed biofilm of VRSA, through in vitro and in vivo experiments.

Curcumin mediated antimicrobial photodynamic therapy was proved to be highly effective in eliminating vancomycin resistant *Staphylococcus aureus* (VRSA) biofilm. Earlier studies on planktonic *S. aureus* have shown that curcumin activity is significantly improved in the presence of blue LED light irradiation at the wavelength of 470 nm [44].

Preliminary in vitro studies of curcumin mediated aPDT against

VRSA were carried out with MIC and MBC, wherein MIC and MBC of only curcumin treated group were found to be 5000 µg/ml and > 5000 µg/ml, respectively, as compared to MIC and MBC of curcumin with light treated group (156.25 µg/ml and 312.5 µg/ml, respectively) (Table 1). Considering the cytotoxic effects of curcumin on human cells followed by laser irradiation, THP-1 cells were exposed to different concentrations (39 µg/ml, 78 µg/ml and 400 µg/ml) of curcumin. Even at a higher concentration (400 µg/ml), the cellular viability of curcumin along with light irradiation was found to be >52% after 24 h of incubation as observed in MTT assay (Fig. 6). Hence, the concentration and exposure time of blue laser light used in this study was found to be non-toxic.

Curcumin mediated antimicrobial photodynamic therapy possesses dual properties such as the direct antibacterial activity of curcumin itself as well as its ROS-mediated effect upon blue light irradiation [44]. In antimicrobial photodynamic therapy, killing or cellular damage is directly proportional to the amount of ROS produced. Therefore, we have checked total intracellular ROS generation by DCFH-DA. An



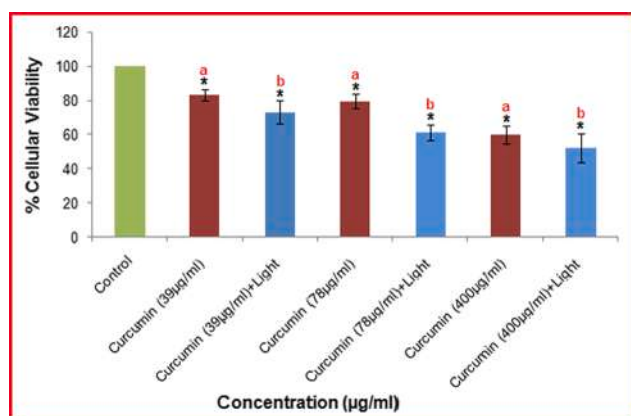


**Fig. 6.** MTT assay: Cytotoxicity of curcumin mediated aPDT on human monocytic cell line (THP1). Data are presented as mean  $\pm$  SD ( $n = 3$ ). Test groups were compared with the control group using the Student's  $t$ -test and one-way analysis of variance (ANOVA) was used for the comparison of multiple means. Data with  $p$ -value of  $<0.05$  (\* $p < 0.01$ , \*\* $p < 0.001$ , \*\*\* $p < 0.0001$ ) was considered statistically significant. a - Only curcumin treated group compared with control or untreated group; b - Curcumin + light treated group compared with control or untreated group.

esterase enzyme causes hydrolysis of DCFH-DA to DCFH, which is further oxidized in the presence of ROS to produce a fluorescent compound DCF. Our data showed significant increase in the intracellular ROS production in curcumin-aPDT treated group as compared to those treated with curcumin alone (Fig. 1) which is in accordance with the data obtained by Jiang *et al.*, 2014, who has demonstrated that, blue light activated curcumin, causing excessive accumulation of

intracellular ROS, leads to loss of VRSA cells.

The mechanism of action involved in antimicrobial photodynamic therapy is merely dependent upon the ability of a photosensitizer to generate ROS such as free radical ( $\text{HO}^\bullet$ ,  $\text{H}_2\text{O}_2$  and  $\text{O}_2^\bullet-$  via type I mechanism) and  $^1\text{O}_2$  (via type II mechanism), when irradiated with light. In order to check the presence of  $\text{HO}^\bullet$  (Type I photochemistry), we have used HPF fluorescence compound, specific for the quantification of hydroxyl radical. Our data showed fluorescence quenching in the group treated with curcumin (78  $\mu\text{g}/\text{ml}$ ) alone as compared to curcumin-aPDT treated group (Fig. 2A). Hence, we further quantify the production of singlet oxygen (Type II photochemistry). We have used AMDA which shows three distinctive absorption bands at 399 nm, 378 nm and 359 nm. The decrease in the absorption at 399 nm is proportional to the amount of  $^1\text{O}_2$  being produced [72]. Our data showed higher amount of  $^1\text{O}_2$  generation in curcumin mediated aPDT treated group as compared to curcumin alone (Fig. 2B). This confirms that singlet oxygen ( $^1\text{O}_2$ ) causes detrimental effects on VRSA cells as compared to hydroxyl radicals. The bacterial cell have sufficient amount of scavengers such as catalase, peroxidase and superoxide dismutase to thwart the free radical mediated bactericidal activity, however they have no remedy against the singlet oxygen molecule, as a result,  $^1\text{O}_2$  leads to maximum cell damage [73]. Biofilms forming bacteria are difficult to treat, since it protects the microorganisms from antibiotics and other antimicrobial agents leading to develop drug resistance [50,74–75]. One of the most pathogenic biofilm-forming bacteria is *Staphylococcus aureus*. In the present study, we have examined whether curcumin mediated aPDT affects preformed biofilm of VRSA. Fig. 3 shows that curcumin-aPDT significantly reduced preformed biofilm of VRSA at a concentration of 78  $\mu\text{g}/\text{ml}$  of curcumin and 20  $\text{J}/\text{cm}^2$  laser irradiation which correspond to 52 s. 3.05  $\log_{10}$  reduction was observed in curcumin-aPDT treated group as compared to 1.19  $\log_{10}$  reduction in only curcumin treated

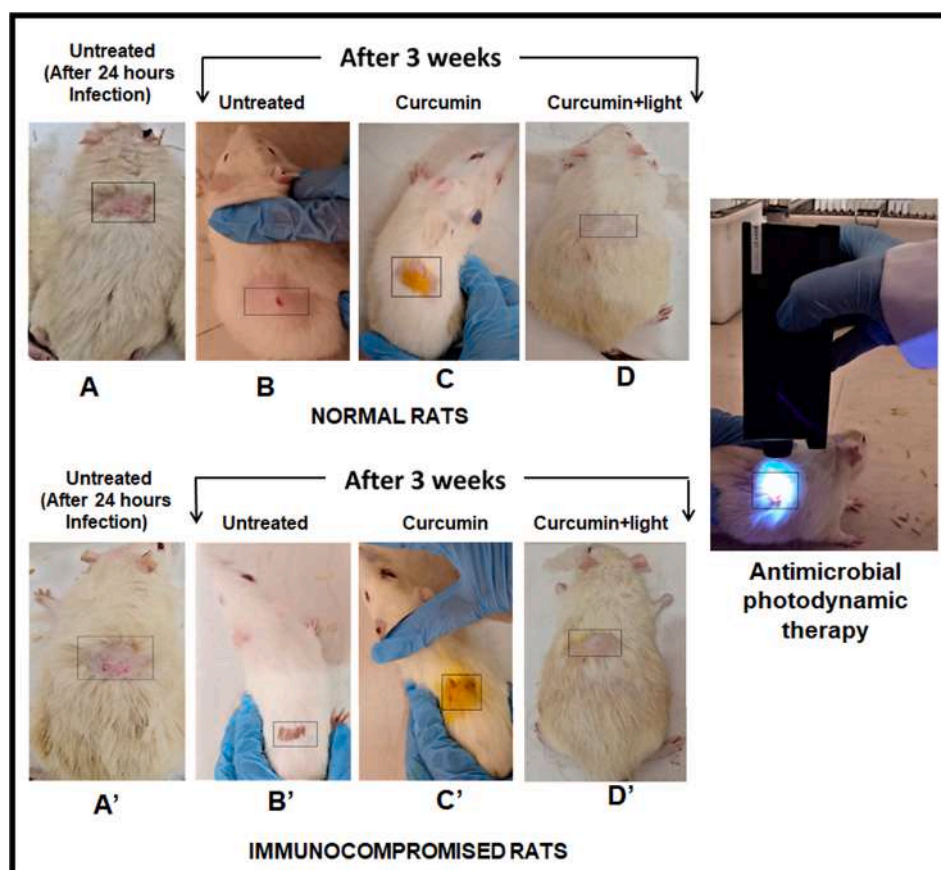


**Fig. 7.** Male wistar rat model of skin abrasion and its treatment.



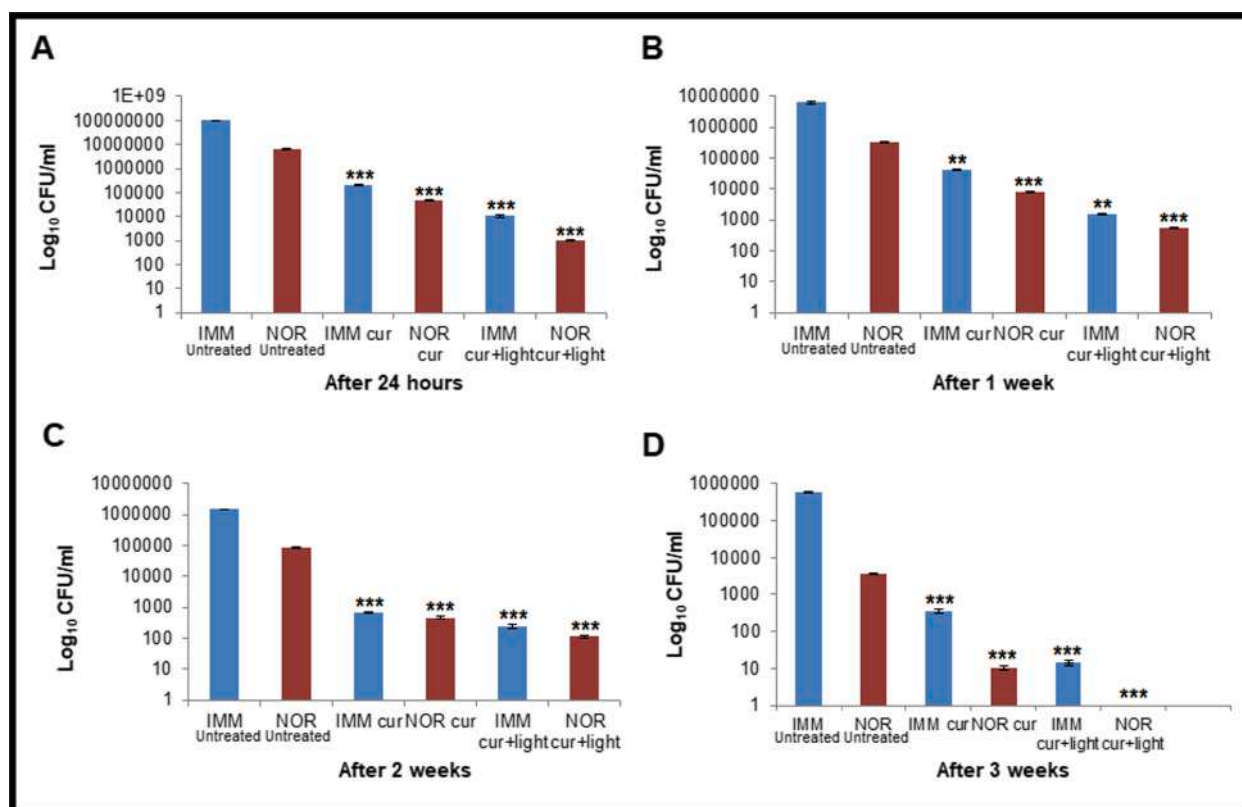


**Fig. 8.** Bacterial load reduction in normal and immunocompromised male wistar rats. (A) CFU/ml after 24 h of post infection, (B) CFU/ml after 1 week of post infection and treatment, (C) CFU/ml after 2 weeks of post infection and treatment and (D) CFU/ml after 3 weeks of post infection and treatment. IMM untreated: immunocompromised untreated rats; NOR untreated: normal untreated rats; IMM cur: immunocompromised rats treated with curcumin only; NOR cur: normal rats treated with curcumin only; IMM cur + light: immunocompromised rats treated with curcumin followed by 20 J/cm<sup>2</sup> of light treatment; NOR cur + light: normal rats treated with curcumin followed by 20 J/cm<sup>2</sup> of light treatment. Data are presented as mean  $\pm$  SD (n = 5). Test groups were compared with the control group using the Student's *t*-test and one-way analysis of variance (ANOVA). Data with p-value of <0.05 (\*p < 0.01, \*\*p < 0.001, \*\*\*p < 0.0001) was considered statistically significant.

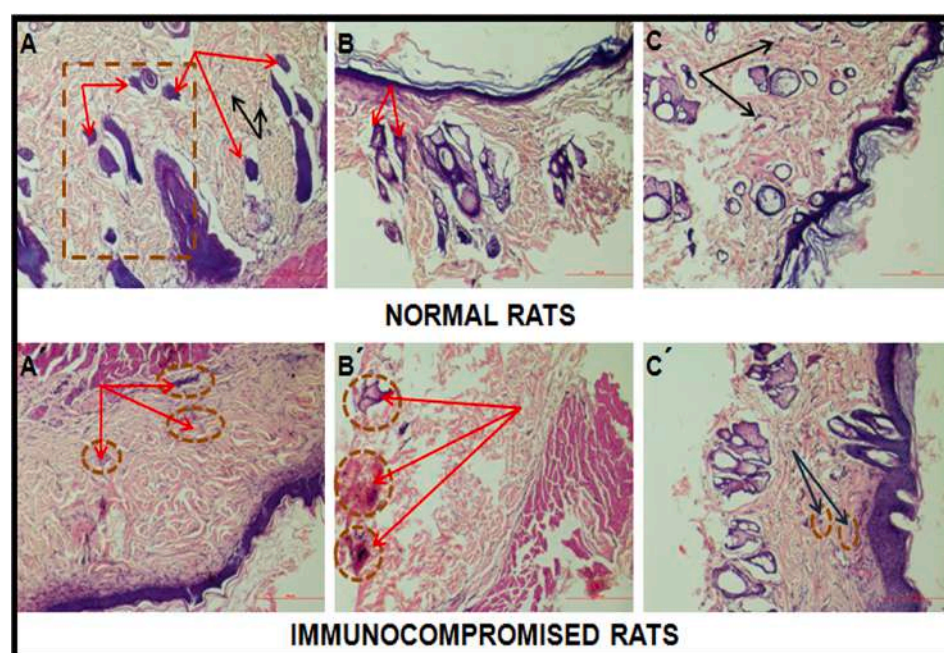


**Fig. 9.** Histopathological investigation by haematoxylin and eosin (H/E) staining to examine response to microorganism. Scale bar = 500  $\mu$ m. Normal rats: (A) Untreated, (B) Only curcumin treated and (C) Curcumin + Light treated. Immunocompromised rats: (A') Untreated, (B') only curcumin treated and (C') Curcumin + light treated groups respectively. Untreated: rats without any treatment after 3 weeks of post infection. Note: Brown dashed line indicates site of infection. Red arrow indicates focal dense neutrophilic infiltrate, black arrow indicates dispersed or scattered neutrophilic infiltrate while blue arrow indicates mild neutrophilic infiltrate. (For interpretation of the references to colour in this figure legend, the reader is referred to the web version of this article.)

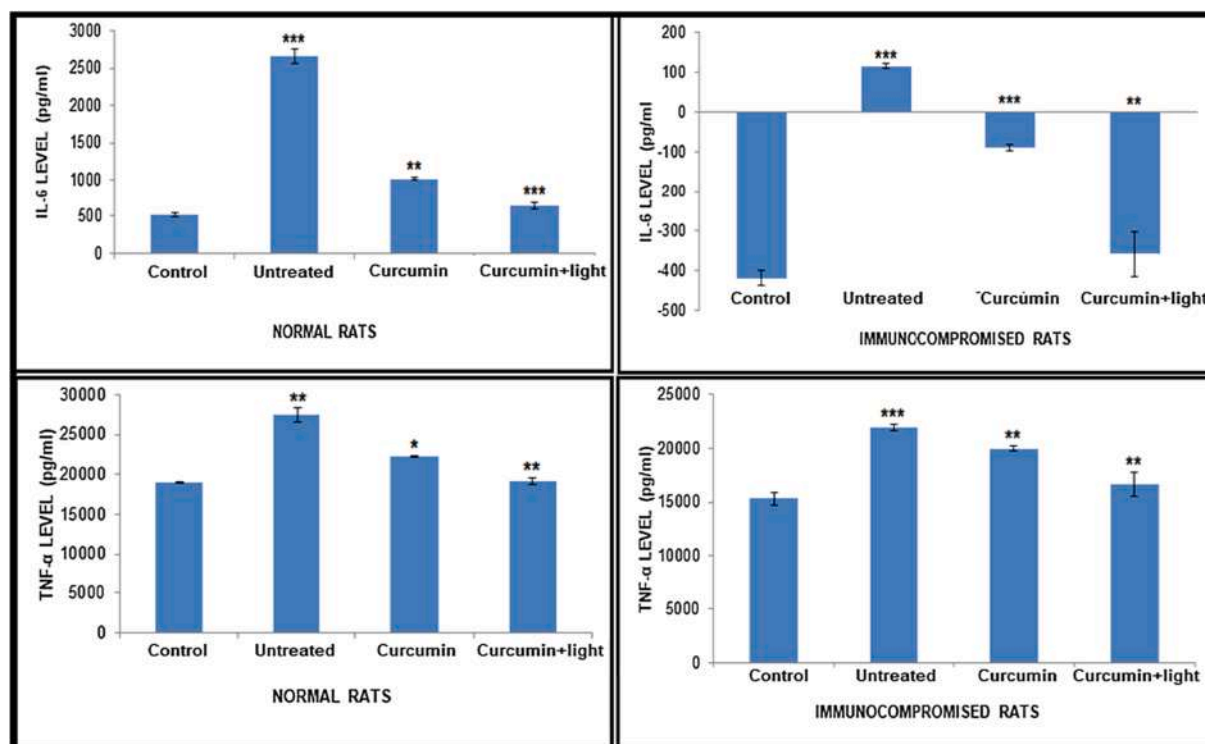


**Fig. 10.** Anti-inflammatory effects of curcumin mediated aPDT in a rat model of Skin abrasion. Normal rats: (A) Level of IL-6 and (B) Level of TNF- $\alpha$ . Immunocompromised rats: (A') Level of IL6 and (B') Level of TNF- $\alpha$  respectively. Data are presented as mean  $\pm$  SD (n = 5). Test groups were compared with the control group using the Student's t-test and one-way analysis of variance (ANOVA) was used for the comparison of multiple means. Data with p-value of  $<0.05$  (\*p < 0.01, \*\*p < 0.001, \*\*\*p < 0.0001) was considered statistically significant.

group. This shows that curcumin mediated aPDT could be sufficient to inhibit biofilm forming VRSA.

Curcumin mediated aPDT results in reduced microbial biomasses as well as EPS production which are of considerable importance for the construction of biofilm architecture [76]. Reduction in biofilm formation was found to be 37.32% in the presence of curcumin, whereas, 67.73% reduction was observed at sub-MIC (78  $\mu$ g/ml) of curcumin with light irradiation, as compared to control (Fig. 4A). EPS reduction at sub-MIC (78  $\mu$ g/ml) concentration of curcumin with light was found to be 47.94%, whereas 13.66% reduction was observed in only curcumin treated group as evaluated by Congo red assays (Fig. 4B).

Furthermore, XTT assay was performed to determine the number of viable cells present after aPDT treatment. Reduced viability was seen when preformed biofilm of VRSA was treated with curcumin mediated aPDT as compared to curcumin alone. Our data revealed that majority of the cells in the biofilm were found to be metabolically active but unable to form a biofilm. This may be due to the inhibitory action of curcumin mediated aPDT (Supplementary figure S2).

Microscopic studies revealed that curcumin mediated aPDT altered the phenotype of the VRSA biofilm. CLSM micrographs illustrate greater disruption of biofilm architecture in curcumin-aPDT treated groups i.e., many bacterial cells were found to be dead (red) within the preformed biofilm of VRSA (Fig. 5C). Thereby demonstrating curcumin-aPDT exhibits strong antimicrobial action against VRSA biofilm. This observation was further supported by the scanning electron microscopy. Unlike the untreated cells (Fig. 5D), with larger cellular aggregates, the treated cells showed detrimental effects on cell wall with significant dispersion of the cells leading to leakage of the cellular content, thus obliterating the structural integrity of a biofilm (Fig. 5F).

We have also examined the effect of curcumin mediated aPDT in rat model of skin abrasion. The result showed daily topical exposure of curcumin followed by light irradiation led to marked reduction of VRSA in normal as well as in immunocompromised rats (Figs. 7 and 8). This

finding is supported by previous study where pronounced reduction in soft-tissue infection with methicillin-resistant *S. aureus* (MRSA), has been observed after aPDT treatment [55]. In addition, the result of histopathological investigation represents complete bacterial clearance with no visible bacterial colonies in curcumin-aPDT treated wound of normal and immunocompromised rats (Fig. 9) [56]. Furthermore, we have checked the immune-protective role of curcumin-aPDT in infection control by proinflammatory cytokines (TNF- $\alpha$  and IL-6) profiling. Cytokines are the soluble glycoproteins possessing several immune functions [77]. Th1 and Th2 cells are the two main subsets of CD4<sup>+</sup> T helper cells. Both the cells maintain a relatively balanced state and secrete different types of cytokines. However, any disturbances in Th1 and Th2 immune responses lead to various diseases. Th1 immune responses induce inflammatory bowel diseases [78], while Th2 immune responses are associated with atopic diseases [79]. In our study, the level of cytokines in normal rats as well as in immunocompromised rats was found to be reduced dramatically after curcumin-aPDT treatment. Furthermore, our results showed that curcumin mediated aPDT restores immunosuppression and improves immunity by augmenting the production of cytokines (Fig. 10).

## 5. Conclusions

This is the first time we have successfully cured VRSA induced skin infection, both in normal and immunocompromised wistar rats using curcumin mediated aPDT. Hence, we proposed that curcumin mediated aPDT could be used against multi-drug resistant bacterial infections and preformed biofilm formation as a potential therapeutic approach (Graphical abstract).

## Declaration of Competing Interest

The authors declare that they have no known competing financial

interests or personal relationships that could have appeared to influence the work reported in this paper.

### Acknowledgements

We are grateful to Dr. Dhiraj Kumar and Dr. Varthika Sharma, Cellular Immunology group, ICGEB, New Delhi, for providing cell culture facilities. We acknowledge Professor Shabbir Ahmed, Department of Physics, AMU, for providing laser. The authors would also like to acknowledge university sophisticated instruments facility (USIF), AMU, for providing instrumental support.

### Funding

This work was supported by Department of Science and Technology Research grant, DST: SR/NM/NS-41/2016(G). FA acknowledged fellowship from Council of Scientific and industrial research: 09/112 (0600)/2018-EMR-I.

### Appendix A. Supplementary data

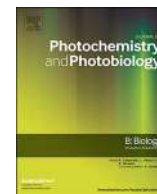
Supplementary data to this article can be found online at <https://doi.org/10.1016/j.ejpb.2021.01.012>.

### References

- [1] S. Hasan, S.Z. Ali, A.U. Khan, Novel combinations of antibiotics to inhibit extended spectrum  $\beta$ -lactamase and metallo- $\beta$ -lactamase producers in vitro: a synergistic approach, *Future Microbiol.* 8 (2013) 939–944.
- [2] M. Krishnamurthy, M.M. Lemmon, E.M. Falcinelli, R.A. Sandy, J.N. Dootz, T. M. Mott, S. Rajamani, K.E. Schaecher, A.J. Duplantier, R.G. Panchal, Enhancing the antibacterial activity of polymyxins using a nonantibiotic drug, *Infect. Drug Resist.* 12 (2019) 1393–1405.
- [3] L.M. de Freitas, E.N. Lorenzón, N.A. Santos-Filho, L.H.d.P. Zago, M.P. Uliana, K.T. de Oliveira, E.M. Cilli, C.R. Fontana, Antimicrobial Photodynamic therapy enhanced by the peptide aurein 1.2, *Scient. Reports*, 8 (2018).
- [4] S. Khan, S.N. Khan, F. Akhtar, L. Misba, R. Meena, A.U. Khan, Inhibition of multi-drug resistant *Klebsiella pneumoniae*: Nanoparticles induced photoinactivation in presence of efflux pump inhibitor, *Eur. J. Pharm. Biopharm.* 157 (2020) 165–174.
- [5] Q.Q. Yang, A.K. Farha, G. Kim, K. Gul, R.Y. Gan, H. Corke, Antimicrobial and anticancer applications and related mechanisms of curcumin-mediated photodynamic treatments, *Trends Food Sci. Technol.* 97 (2020) 341–354.
- [6] H. Chen, H. Deng, X. Zou, J. Zhao, Hypocrellin B Encapsulated in Triphenyl Phosphonium-Modified Cationic Liposomes for Photodynamic Treatment of Exudative Age-Related Macular Degeneration, *J. Biomed. Nanotechnol.* 15 (2019) 2305–2320.
- [7] Ursula Schmidt-Erfurth, Tayyaba Hasan, Mechanisms of action of photodynamic therapy with verteporfin for the treatment of age-related macular degeneration, *Surv. Ophthalmol.* 45 (3) (2000) 195–214.
- [8] M. Gallardo-Villagrán, D.Y. Leger, B. Liagre, B. Therrien, Photosensitizers Used in the Photodynamic Therapy of Rheumatoid Arthritis, *Int. J. Mol. Sci.* 20 (2019) 3339.
- [9] M.A.A. Freitas, A.H.C. Pereira, J.G. Pinto, A. Casas, J. Ferreira-Strixino, Bacterial viability after antimicrobial photodynamic therapy with curcumin on multiresistant *Staphylococcus aureus*, *Future Microbiol.* 14 (2019) 739–748.
- [10] Y. Panahi, O. Fazlollahzadeh, S.L. Atkin, M. Majeed, A.E. Butler, T.P. Johnston, A. Sahebkar, Evidence of curcumin and curcumin analogue effects in skin diseases: A narrative review, *J. Cell. Physiol.* 234 (2018) 1165–1178.
- [11] T.M. Branco, N.C. Valério, V.I.R. Jesus, C.J. Dias, M.G.P.M.S. Neves, M.A. Faustino, A. Almeida, Single and combined effects of photodynamic therapy and antibiotics to inactivate *Staphylococcus aureus* on skin, *Photodiagn. Photodyn. Ther.* 21 (2018) 285–293.
- [12] W. Kałas, E. Wysokińska, M. Przybyło, M. Langner, A. Ulatowska-Jarża, D. Biały, M. Wawrzyńska, E. Ziolo, W. Gil, A.M. Trzeciak, H. Podbielska, M. Kopaczynska, Photoactive Liposomal Formulation of PVP-Conjugated Chlorin e6 for Photodynamic Reduction of Atherosclerotic Plaque, *Int. J. Mol. Sci.* 20 (2019) 3852.
- [13] L. Costa, M.A.F. Faustino, J.P.C. Tomé, M.G.P.M.S. Neves, A.C. Tomé, J.A. S. Cavaleiro, A. Cunha, A. Almeida, Involvement of type I and type II mechanisms on the photoinactivation of non-enveloped DNA and RNA bacteriophages, *J. Photochem. Photobiol.*, B 120 (2013) 10–16.
- [14] C.M.B. Carvalho, A.T.P.C. Gomes, S.C.D. Fernandes, A.C.B. Prata, M.A. Almeida, M. A. Cunha, J.P.C. Tomé, M.A.F. Faustino, M.G.P.M.S. Neves, A.C. Tomé, J.A. S. Cavaleiro, Z. Lin, J.P. Rainho, J. Rocha, Photoinactivation of bacteria in wastewater by porphyrins: Bacterial  $\beta$ -galactosidase activity and leucine-uptake as methods to monitor the process, *J. Photochem. Photobiol.*, B 88 (2007) 112–118.
- [15] A. Almeida, M.A.F. Faustino, J.P.C. Tomé, Photodynamic inactivation of bacteria: finding the effective targets, *Future Med. Chem.* 7 (2015) 1221–1224.
- [16] M.R. Hamblin, T. Hasan, Photodynamic therapy: a new antimicrobial approach to infectious disease? *Photochem. Photobiol. Sci.* 3 (5) (2015) 436–450.
- [17] L. Costa, M.A.F. Faustino, M.G.P.M.S. Neves, A. Cunha, A. Almeida, Photodynamic Inactivation of Mammalian Viruses and Bacteriophages, *Viruses* 4 (2012) 1034–1074.
- [18] R.N. da Silva, A.C. Tomé, J.P.C. Tomé, M.G.P.M.S. Neves, M.A.F. Faustino, J.A. S. Cavaleiro, A. Oliveira, A. Almeida, A. Cunha, Photo-inactivation of *Bacillus endospores*: inter-specific variability of inactivation efficiency, *Microbiol. Immunol.* 56 (2012) 692–699.
- [19] T. Maisch, C. Bosl, R.M. Szeimies, B. Love, C. Abels, Determination of the antibacterial efficacy of a new porphyrin-based photosensitizer against MRSA *ex vivo*, *Photochem. Photobiol. Sci.* 6 (2007) 545.
- [20] G.B. Rodrigues, L.K.S. Ferreira, M. Wainwright, G.U.L. Braga, Susceptibilities of the dermatophytes *Trichophyton mentagrophytes* and *T. rubrum* microconidia to photodynamic antimicrobial chemotherapy with novel phenothiazinium photosensitizers and red light, *J. Photochem. Photobiol.*, B 116 (2012) 89–94.
- [21] G.B. Rodrigues, M. Dias-Baruffi, N. Holman, M. Wainwright, G.U.L. Braga, *In vitro* photodynamic inactivation of *Candida* species and mouse fibroblasts with phenothiaziniumphotosensitisers and red light, *Photodiagn. Photodyn. Ther.* 10 (2013) 141–149.
- [22] Sandra Beirao, S. Fernandes, J. Coelho, M.A.F. Faustino, J.P.C. Tome, M. Neves, A. C. Tome, A. Almeida, A. Cunha, Photodynamic inactivation of bacterial and yeast biofilms with a cationic porphyrin, *Photochem. Photobiol.* 90 (6) (2014) 1387–1396.
- [23] R. Fekrazad, Photobiomodulation and Antiviral Photodynamic Therapy as a Possible Novel Approach in COVID-19 Management, *Photobiomodul., Photomed., Laser Surg.* 38 (2020) 255–257.
- [24] R.R. Allison, C.H. Sibata, Oncologic photodynamic therapy photosensitizers: A clinical review, *Photodiagn. Photodyn. Ther.* 7 (2010) 61–75.
- [25] H. Abrahamse, R. Michael, Hamblin, New photosensitizers for photodynamic therapy, *Biochem. J.* 473 (2016) 347–364.
- [26] H. Chung, T. Dai, S.K. Sharma, Y.-Y. Huang, J.D. Carroll, M.R. Hamblin, The Nuts and Bolts of Low-level Laser (Light) Therapy, *Ann. Biomed. Eng.* 40 (2011) 516–533.
- [27] Liyi Huang, et al., Paradoxical potentiation of methylene blue-mediated antimicrobial photodynamic inactivation by sodium azide: role of ambient oxygen and azide radicals, *Free Radical Biol. Med.* 53 (11) (2012) 2062–2071.
- [28] Mauricio S. Baptista, et al., Type I and type II photosensitized oxidation reactions: guidelines and mechanistic pathways, *Photochem. Photobiol.* 93 (4) (2017) 912–919.
- [29] R. Tao, F. Zhang, Q.-J. Tang, C.-S. Xu, Z.-J. Ni, X.-H. Meng, Effects of curcumin-based photodynamic treatment on the storage quality of fresh-cut apples, *Food Chem.* 274 (2019) 415–421.
- [30] C.C.C. Quishida, E.G. De Oliveira Mima, J.H. Jorge, C.E. Vergani, V.S. Bagnato, A. C. Pavarina, Photodynamic inactivation of a multispecies biofilm using curcumin and LED light, *Lasers Med. Sci.* 31 (2016) 997–1009.
- [31] M. Mirzahasseinipour, K. Khorsandi, R. Hosseinzadeh, M. Ghazaeian, F.K. Shahidi, Antimicrobial photodynamic and wound healing activity of curcumin encapsulated in silica nanoparticles, *Photodiagn. Photodyn. Ther.* 29 (2020), 101639.
- [32] D. Praditya, L. Kirchhoff, J. Brüning, H. Rachmawati, J. Steinmann, E. Steinmann, Anti-infective Properties of the Golden Spice Curcumin, *Front. Microbiol.* 10 (2019).
- [33] W.H. Tsai, K.-H. Yu, Y.-C. Huang, C.-I. Lee, EGFR-targeted photodynamic therapy by curcumin-encapsulated chitosan/TPP nanoparticles, *Int. J. Nanomed.* 13 (2018) 903–916.
- [34] R.K. Maheshwari, A.K. Singh, J. Gaddipati, R.C. Simal, Multiple biological activities of curcumin: A short review, *Life Sci.* 78 (2006) 2081–2087.
- [35] G. Bar-Sela, R. Epelbaum, M. Schaffer, Curcumin as an Anti-Cancer Agent: Review of the Gap Between Basic and Clinical Applications, *Curr. Med. Chem.* 17 (2010) 190–197.
- [36] P. Basnet, N. Skalko-Basnet, Curcumin: An Anti-Inflammatory Molecule from a Curry Spice on the Path to Cancer Treatment, *Molecules* 16 (2011) 4567–4598.
- [37] T. Hamaguchi, K. Ono, M. Yamada, REVIEW: Curcumin and Alzheimer's Disease, *CNS Neurosci. Ther.* 16 (2010) 285–297.
- [38] A. Federico, E. Cardaioli, P. Da Pozzo, P. Formichi, G.N. Gallus, E. Radi, Mitochondria, oxidative stress and neurodegeneration, *J. Neurol. Sci.* 322 (2012) 254–262.
- [39] V. Sakima, P. Barbugli, P. Cerri, M. Chorilli, J. Carmello, A. Pavarina, E. Mima, Antimicrobial Photodynamic Therapy Mediated by Curcumin-Loaded Polymeric Nanoparticles in a Murine Model of Oral Candidiasis, *Molecules* 23 (2018) 2075.
- [40] D. Akbik, M. Ghadiri, W. Chrzanowski, R. Rohanzadeh, Curcumin as a wound healing agent, *Life Sci.* 116 (2014) 1–7.
- [41] B. Fonseca-Santos, A.M. dos Santos, C.F. Rodero, M.P.D. Gremião, M. Chorilli, Design, characterization, and biological evaluation of curcumin-loaded surfactant-based systems for topical drug delivery, *Int. J. Nanomed.* 11 (2016) 4553–4562.
- [42] S. Tejeda, A. Manayi, M. Daglia, S.F. Nabavi, A. Sureda, Z. Hajheydari, O. Gortzi, H. Pazoki-Toroudi, S.M. Nabavi, Wound Healing Effects of Curcumin: A Short Review, *Curr. Pharm. Biotechnol.* 17 (2016) 1002–1007.
- [43] Z. Hussain, H.E. Thu, S.-F. Ng, S. Khan, H. Katas, Nanoencapsulation, an efficient and promising approach to maximize wound healing efficacy of curcumin: A review of new trends and state-of-the-art, *Colloids Surf., B* 150 (2017) 223–241.
- [44] Y. Jiang, A.W. Leung, H. Hua, X. Rao, C. Xu, Photodynamic Action of LED-Activated Curcumin against *Staphylococcus aureus* Involving Intracellular ROS Increase and Membrane Damage, *Int. J. Photoenergy* 2014 (2014) 1–7.



- [45] T. Dai, G.P. Tegos, T. Zhiyentayev, E. Mylonakis, M.R. Hamblin, Photodynamic therapy for methicillin-resistant *Staphylococcus aureus* infection in a mouse skin abrasion model, *Lasers Surg. Med.* 42 (2010) 38–44.
- [46] S. Khan, F. Alam, A. Azam, A.U. Khan, Gold nanoparticles enhance methylene blue induced photodynamic therapy: a novel therapeutic approach to inhibit *Candida albicans* biofilm, *Int. J. Nanomed.* 3245 (2012).
- [47] J.P.M.L. Rollim, M.A.S. de-Melo, S.F. Guedes, F.B. Albuquerque-Filho, J.R. de Souza, N.A.P. Nogueira, I.C.J. Zanin, L.K.A. Rodrigues, The antimicrobial activity of photodynamic therapy against *Streptococcus mutans* using different photosensitizers, *J. Photochem. Photobiol. B: Biol.* 106 (2012) 40–46.
- [48] L. Misba, S. Kulshrestha, A.U. Khan, Antibiofilm action of a toluidine blue O-silver nanoparticle conjugate on *Streptococcus mutans*: a mechanism of type I photodynamic therapy, *Biofouling* 32 (2016) 313–328.
- [49] K.R. Kasimova, M. Sadasivam, G. Landi, T. Sarna, M.R. Hamblin, Potentiation of photoinactivation of Gram-positive and Gram-negative bacteria mediated by six phenothiazinium dyes by addition of azide ion, *Photochem. Photobiol. Sci.* 13 (2014) 1541–1548.
- [50] J. Chen, T.C. Cesario, P.M. Rentzepis, Rationale and mechanism for the low photoinactivation rate of bacteria in plasma, *Proc. Natl. Acad. Sci.* 111 (2013) 33–38.
- [51] L. Misba, S. Zaidi, A.U. Khan, A comparison of antibacterial and antibiofilm efficacy of phenothiazinium dyes between Gram positive and Gram negative bacterial biofilm, *Photodiagn. Photodyn. Ther.* 18 (2017) 24–33.
- [52] A. López-Moreno, J.D. Sepúlveda-Sánchez, E.M. Mercedes Alonso Guzmán, S. Le Borgne, Calcium carbonate precipitation by heterotrophic bacteria isolated from biofilms formed on deteriorated ignimbrite stones: influence of calcium on EPS production and biofilm formation by these isolates, *Biofouling*, 30 (2014) 547–560.
- [53] S. Kulshrestha, S. Khan, S. Hasan, M.E. Khan, L. Misba, A.U. Khan, Calcium fluoride nanoparticles induced suppression of *Streptococcus mutans* biofilm: an in vitro and in vivo approach, *Appl. Microbiol. Biotechnol.* 100 (2015) 1901–1914.
- [54] V.A. Senapati, A. Kumar, G.S. Gupta, A.K. Pandey, A. Dhawan, ZnO nanoparticles induced inflammatory response and genotoxicity in human blood cells: A mechanistic approach, *Food Chem. Toxicol.* 85 (2015) 61–70.
- [55] F. Gad, T. Zahra, K.P. Francis, T. Hasan, M.R. Hamblin, Targeted photodynamic therapy of established soft-tissue infections in mice, *Photochem. Photobiol. Sci.* 3 (2004) 451.
- [56] J.H. Park, M.-Y. Ahn, Y.-C. Kim, S.-A. Kim, Y.-H. Moon, S.-G. Ahn, J.-H. Yoon, In Vitro and in Vivo Antimicrobial Effect of Photodynamic Therapy Using a Highly Pure Chlorin e6 against *Staphylococcus aureus* Xen29, *Biol. Pharm. Bull.* 35 (2012) 509–514.
- [57] A.A. Tawfik, I. Noaman, H. El-Elsayyad, N. El-Mashad, M. Soliman, A study of the treatment of cutaneous fungal infection in animal model using photoactivated composite of methylene blue and gold nanoparticle, *Photodiagn. Photodyn. Ther.* 15 (2016) 59–69.
- [58] M. Karamese, H.S. Erol, M. Albayrak, G. Findikguvendi, E. Aydin, S. AksakKaramese, Anti-oxidant and anti-inflammatory effects of apigenin in a rat model of sepsis: an immunological, biochemical, and histopathological study, *Immunopharmacol. Immunotoxicol.* 38 (2016) 228–237.
- [59] ANOVA: ANalysis Of VAriance between groups. [www.physics.csbsju.edu/stats/anova.html](http://www.physics.csbsju.edu/stats/anova.html).
- [60] G.L. Archer, *Staphylococcus aureus*: A Well-Armed Pathogen, *Clin. Infect. Dis.* 26 (1998) 1179–1181.
- [61] A.S. Bayer, A.F. Bolger, K.A. Taubert, W. Wilson, J. Steckelberg, A.W. Karchmer, M. Levison, H.F. Chambers, A.S. Dajani, M.H. Gewitz, J.W. Newburger, M. A. Gerber, S.T. Shulman, T.J. Pallasch, T.W. Gage, P. Ferrieri, Diagnosis and Management of Infective Endocarditis and Its Complications, *Circulation* 98 (1998) 2936–2948.
- [62] B.M. Limbago, A.J. Kallen, W. Zhu, P. Eggers, L.K. McDougal, V.S. Albrecht, Report of the 13th Vancomycin-Resistant *Staphylococcus aureus* Isolate from the United States, *J. Clin. Microbiol.* 52 (2013) 998–1002.
- [63] A. Friães, C. Resina, V. Manuel, L. Lito, M. Ramirez, J. Melo-Cristino, Epidemiological survey of the first case of vancomycin-resistant *Staphylococcus aureus* infection in Europe, *Epidemiol. Infect.* 143 (2014) 745–748.
- [64] P.P. Almeida, Í.S. Pereira, K.B. Rodrigues, L.S. Leal, A.S. Marques, L.P. Rosa, F.C. da Silva, R.A.A. da Silva, Photodynamic therapy controls of *Staphylococcus aureus* intradermal infection in mice, *Lasers Med. Sci.* 32 (2017) 1337–1342.
- [65] D.J. Diekema, B.J. BootsMiller, T.E. Vaughn, R.F. Woolson, J.W. Yankey, E.J. Ernst, S.D. Flach, M.M. Ward, C.L.J. Francis, M.A. Pfaller, B.N. Doebbeling, Antimicrobial Resistance Trends and Outbreak Frequency in United States Hospitals, *Clin. Infect. Dis.* 38 (2004) 78–85.
- [66] S. Projan, Antimicrobials: new solutions badly needed, *Curr. Opin. Microbiol.* 5 (2002) 463–465.
- [67] K. Sieradzki, R.B. Roberts, S.W. Haber, A. Tomasz, The Development of Vancomycin Resistance in a Patient with Methicillin-Resistant *Staphylococcus aureus* Infection, *N. Engl. J. Med.* 340 (1999) 517–523.
- [68] S. Khan, S.N. Khan, R. Meena, A.M. Dar, R. Pal, A.U. Khan, Photoinactivation of multidrug resistant bacteria by monomeric methylene blue conjugated gold nanoparticles, *J. Photochem. Photobiol., B* 174 (2017) 150–161.
- [69] Z.A. Malik, D. Broughel, The importance of testing whole stool for Shiga toxin: a clinical and microbiological perspective, *J.-Pakistan Med. Assoc.* 57 (5) (2007) 265.
- [70] G.P. Tegos, M. Anbe, C. Yang, T.N. Demidova, M. Satti, P. Mroz, S. Janjua, F. Gad, M.R. Hamblin, Protease-Stable Polycationic Photosensitizer Conjugates between Polyethyleneimine and Chlorin(e6) for Broad-Spectrum Antimicrobial Photoinactivation, *Antimicrob. Agents Chemother.* 50 (2006) 1402–1410.
- [71] M.R. Hamblin, Polycationic photosensitizer conjugates: effects of chain length and Gram classification on the photodynamic inactivation of bacteria, *J. Antimicrob. Chemother.* 49 (2002) 941–951.
- [72] G.A. Pankey, L.D. Sabath, Clinical Relevance of Bacteriostatic versus Bactericidal Mechanisms of Action in the Treatment of Gram-Positive Bacterial Infections, *Clin. Infect. Dis.* 38 (2004) 864–870.
- [73] S.Y. Kim, O.J. Kwon, J.-W. Park, Inactivation of catalase and superoxide dismutase by singlet oxygen derived from photoactivated dye, *Biochimie* 83 (2001) 437–444.
- [74] C. Liu, Y. Zhou, L. Wang, L. Han, J.e. Lei, H.M. Ishaq, S.P. Nair, J. Xu, Photodynamic inactivation of *Klebsiella pneumoniae* biofilms and planktonic cells by 5-aminolevulinic acid and 5-aminolevulinic acid methyl ester, *Lasers Med. Sci.*, 31 (2016) 557–565.
- [75] A. Zuberi, N. Ahmad, A.U. Khan, CRISPRi Induced Suppression of Fimbriae Gene (fimH) of a Uropathogenic *Escherichia coli*: An Approach to Inhibit Microbial Biofilms, *Front. Immunol.* 8 (2017).
- [76] H.C. Flemming, J. Wingender, The biofilm matrix, *Nat. Rev. Microbiol.* 8 (2010) 623–633.
- [77] J.J. Burns, L. Zhao, E.W. Taylor, K. Spelman, The influence of traditional herbal formulas on cytokine activity, *Toxicology* 278 (2010) 140–159.
- [78] J. Šventoraitytė, A. Žvirblienė, G. Kiudelis, R. Žalinskius, A. Žvirblienė, A. Práškevičius, L. Kupčinskis, V. Tamošiūnas, Immune system alterations in patients with inflammatory bowel disease during remission, *Medicina* 44 (2008) 27.
- [79] J.V. Fahy, Type 2 inflammation in asthma present in most, absent in many, *Nat. Rev. Immunol.* 15, (1) (2015) 57–65.



# Photoinactivation of multidrug resistant bacteria by monomeric methylene blue conjugated gold nanoparticles



Shakir Khan<sup>a</sup>, Shahper N. Khan<sup>a</sup>, Ramovatar Meena<sup>c</sup>, Ayaz M. Dar<sup>b</sup>, Ruchita Pal<sup>d</sup>, Asad U. Khan<sup>a,\*</sup>

<sup>a</sup> Interdisciplinary Biotechnology Unit, Aligarh Muslim University, Aligarh 202002, India

<sup>b</sup> Department of Chemistry, Aligarh Muslim University, Aligarh 202002, India

<sup>c</sup> School of Environmental Sciences, Jawaharlal Nehru University, New Delhi 110067, India

<sup>d</sup> Advanced Instrumentation Research Facility, Jawaharlal Nehru University, New Delhi 110067, India

## A B S T R A C T

Multidrug resistant (MDR) bacterial infections have become a severe threat to the community health due to a progressive rise in antibiotic resistance. Nanoparticle-based photodynamic therapy (PDT) is increasingly been adopted as a potential antimicrobial option, yet the cytotoxicity associated with PDT is quite unspecific. Herein, we show Concanavalin-A (ConA) directed dextran capped gold nanoparticles (GNP<sub>DEX</sub>-ConA) enhanced the efficacy and selectivity of methylene blue (MB) induced killing of multidrug resistant clinical isolates. Here, we show that our complex MB@GNP<sub>DEX</sub>-ConA is effective against range of MDR clinical isolates, including *Escherichia coli*, *Klebsiella pneumoniae* and *Enterobacter cloacae*. In our treatment modality negligible dark toxicity suggests photochemically driven process with 97% killing of MDR bacteria. GNP<sub>DEX</sub>-ConA with monomeric form of MB departs maximum fluorescence decay time ( $\tau$ : 1.7 ns in HSA) and singlet oxygen ( $\Delta\Phi$ ; 0.84) for improved activity in albumin rich infection sites. Further, the complex show least toxicity when tested against HEK293 mammalian cells. The principle component analysis (PCA) and confocal microscopy illustrates cytosolic <sup>1</sup>O<sub>2</sub> mediated type-II PDT as mechanism of action. Hence, MB@GNP<sub>DEX</sub>-ConA mediated PDT is potential therapeutic approach against MDR infections and can be tailored to fight other infectious diseases.

## 1. Introduction

Inordinate and injudicious prescription of last resort antibiotics has driven the expansion of bacterial resistance toward  $\beta$ -lactam groups of antibiotics [1–3]. Inevitably, since last decade multidrug resistance (MDR) has emerged as a global prophylactic hindrance for the community and nosocomially acquired infections [3]. The ‘super-enzyme’, a variant of bacterial metallo- $\beta$ -lactamases (MBLs) called carbapenemase first reported in a clinical MDR samples in 2008. Since then, the frequency of super enzyme is increasing continually around the world especially in Enterobacteriaceae family such as *Escherichia coli*, *Klebsiella pneumoniae* and *Enterobacter cloacae* [4,5]. Recently, 2013 Centers for Disease Control report the alarmingly progressive spread of antibiotic-resistant ‘superbugs’ nearly two million people that currently killing at least 23,000 people annually in the US alluded to lack of effective antibiotics [6].

Controlling such infections by “multi-loop-whole” mechanism is going to be ineffective, where targeting single virulence factor didn't completely obliterate the major challenges. At the same time, there is a shortage in terms of the development of newer antibiotics against MDR

bacteria [7], and so new strategies are imperative to cure these prolific infections. Recently, photodynamic therapy (PDT) has been demonstrated multipronged strategy, which is far most effective in the inactivation of microorganisms such as bacteria, yeast, fungi, and viruses [8–11], as compared to almost single targeted  $\beta$ -lactam groups of antibiotics. PDT as a treatment modality is based on the action of light on a non-toxic photosensitizer (PS) that leads to the production of reactive oxygen species toxic to cellular components and metabolism. This approach is as very efficient in killing MDR strains and microorganisms do not develop resistance toward PDT [12,13].

The phenothiazinium dye such as Methylene blue is approved by U.S. food & drug; FDA for the treatment of methanoglobinemia, and used at a much higher concentration (1–2 mg/kg) than normally used in photodynamic therapy [14]. Nevertheless, photo-activated MB shows the photo-cytotoxicity through type-I (produce HO<sup>•</sup>, H<sub>2</sub>O<sub>2</sub> etc.) and/or type-II (produce <sup>1</sup>O<sub>2</sub>) PDT mechanism dependant on the ambient substrates/oxygen and dimeric/monomeric form of MB [15,16]. Hence, this study is further desirable to address the ambiguity of which type of photo-inactivation (type-I/II) is used. In addition, on photosensitization, free PSs are also reported to exhibit therapeutic responses on

\* Corresponding author.

E-mail address: [asad.k@rediffmail.com](mailto:asad.k@rediffmail.com) (A.U. Khan).

bystander healthy host cells [17]. Recently, the nano-deviced photosensitizer is opted to enhance their pharmacokinetic and pharmacodynamic spectrum. Here, Concanavalin-A aggregated dextran capped gold nanoparticles (GNP<sub>DEX</sub>-ConA) were used; first to reduce the PS's indiscriminate host cell attachment for the control of cytotoxicity implication in in vivo setting and second to enhance type-I PDT where "close proximity" as well as monomeric form of PS's around the GNP showed enhanced singlet oxygen generation, resulting in enhanced antimicrobial photo-toxicity [15,18]. Hence, extensive research is directed on specifically targeting bacterial cell for discriminate delivery of the antimicrobials to ensure better results and least unspecific toxicity to the host. In that direction, components of bacterial cell wall i.e. lipopolysaccharides and carbohydrate-specific moieties have been exploited as a target in designing biosensors by researchers for detecting bacterial infections [19,20], where multivalent cooperative interactions between carbohydrate-protein complex ensure stable binding and thereby specificity to a drug carrier/nanoparticles [21]. Herein, the aim of our study is to develop MB@GNP<sub>DEX</sub>-ConA mediated treatment modality against multidrug resistant infections and testing it in Human Serum Albumin (HSA) rich environment to the simulated infection site, where microbes proliferate.

## 2. Materials and Methodology

### 2.1. Materials

Chloroauric acid (HAuCl<sub>4</sub>), Dextran (T-50 grade), Dextran monomer (Methyl- $\alpha$ -D-mannopyranoside), Concanavalin-A (ConA), Methylene Blue (MB), MTT ((3-(4,5-Dimethyl thiazol-2-yl)-2,5-diphenyltetrazolium bromide), XTT (2,3-Bis(2-methoxy-4-nitro-5-sulphophenyl)-5-([phenylamino] carbonyl)-2H-tetrazolium hydroxide), Menadione, Crystal Violet (CV), DAPI (4, 6-diamidino-2-phenylindole), PI (Propidium Iodide) and DCFH-DA (2, 7-Dichlorofluorescein diacetate) were purchased from Sigma-Aldrich, India. Green fluorescent nucleic acid stain (Syto®-9) and Singlet oxygen green sensor reagent (GR) were purchased from Molecular Probes/Invitrogen, India.

### 2.2. Synthesis and Characterization

Dextran-capped gold nanoparticles (GNP<sub>DEX</sub>) were prepared at room temperature (30 °C) by the slightly modified method [22] (Method S1, Supporting Information). Diffraction patterns and crystallinity of GNP<sub>DEX</sub> determined by XRD and validated by HR-TEM and SAED (Selected area electron diffraction) (Method S2, Fig. S2, Table. S1 and S2, Supporting Information). The functional groups involved in types of bonding formation between MB and GNP<sub>DEX</sub> were analyzed by <sup>1</sup>H spectra that were run in CDCl<sub>3</sub> on a JEOL Eclipse (500 MHz) instrument with TMS as internal standard and values are given in ppm ( $\delta$ ) (Method S3, Supporting Information). The methods used during the synthesis and further nano-formulation characterization given in Method S1 (see Supporting Information).

### 2.3. Bacterial Strains and Growth Conditions

NDM-1 producing *Klebsiella pneumoniae* (KP-12, accession number: JN860195.1) and *Enterobacter cloacae* (EC-15, accession number: JN860194.1) strains were isolated from localized diabetic foot ulcer patients and used in this study [23]. The other clinical strains isolated from nosocomial and community-acquired infections were *Escherichia coli* (D295 and D253) and *Klebsiella pneumoniae* (KP113, KP160, KP229, KP277). KPA (*Klebsiella pneumoniae*; ATCC 13883) was used as reference strain. Human embryonic kidney cell line (HEK-293) provided by National Centre for Cell Science (NCCS), India. This study on clinical isolates was reviewed and received ethical approval by the Institutional Ethical Committee, Aligarh Muslim University under registration number 322/CPCSEA. The clinical isolate virulence factors, resistance

mechanism and capability of adherence of KP-12 are listed in the supplementary table (Table S3, Supporting Information). The capability of adherence of clinical isolate was ascertained by Congo Red Agar method (Method S4, Supporting Information). For all these bacterial growth conditions, freshly LB (Luria-Bertani) agar grown single bacterial cell colony was picked and grown in batches of LB media (20 ml in 250 ml Erlenmeyer Flasks) for overnight at 37 °C under aerobic condition. These bacterial cells were harvested and washed thrice with PBS (pH 7.4). Bacterial cell suspension turbidity or cell density ( $6 \times 10^8$  cells ml<sup>-1</sup>) estimated by spectrophotometry (Optical Density; OD 0.4 at 600 nm) corresponding to McFarland standard No. 2 and further confirmed by single cell colony forming (CFU) counts on LB agar plates.

### 2.4. Photosensitization and Microscopic Studies

Bacterial cells were treated with photosensitized MB and MB@GNP<sub>DEX</sub>-ConA in a various media environment. Semiconductor AlGaInP diode laser (Model No-MRL-III-660; CNI, China) with an output power of 100 mW and light source of 660 nm wavelength was used for photosensitization. The comprehensive treatment modality, formulation, and dosimetry are given in data (Method S5 and Table S4, Supporting Information). The methods for achievement of microbial photo-toxicity are illustrated in Fig. S3 (Supporting Information). The methods used in microbial microscopic studies described in Method S6 (Supporting Information).

### 2.5. <sup>1</sup>O<sub>2</sub> Quantum Yield and Fluorescence Decay Measurements

The singlet oxygen generation also confirmed by the chemical method by using Na<sub>2</sub>-ADPA ( $10 \times 10^6$  M) as a singlet oxygen trapping agent [24,25]. The decrease in maximum absorption ( $\lambda_{\text{max}}$  of ADPA; 380 nm) was calculated during the different laser light treatment time (t; 60, 80, 100, and 120 s.). Where, singlet oxygen generated by the photosensitization was trapped on ADPA and decreased  $\lambda_{\text{max}}$  proportional to amount of singlet oxygen formation. The area under the absorption of light ( $A_{\text{abs}}$ ) is proportional to the intensity of light absorbed ( $I_{\text{abs}}$ ) between 500 and 700 nm wavelength ( $\lambda$ ).

Thus, the decay of [ADPA] follows the first-order kinetics:

$$[\text{ADPA}]_t = [\text{ADPA}]_0 \exp(-kt) \quad (1)$$

$$\ln([\text{ADPA}]_t / [\text{ADPA}]_0) = -kt \quad (2)$$

Here, the data were plotted as  $\ln[\text{ADPA}]_t / [\text{ADPA}]_0$  versus irradiation time t, the slope of each sample was obtained after fitting with a linear function (k). The quantification of singlet oxygen quantum yield ( $\Delta\Phi$ ) of nano-conjugates, the following Eq. (3) used. Where MB alone was used as the standard photosensitizer ( $\Delta\Phi_{\text{MB}}$  is 0.52 in water [15]) and the asterisk represents the MB@GNP<sub>DEX</sub>-ConA.

$$\Delta\Phi^{(\text{MB}^*)} = \Delta\Phi_{\text{MB}} \frac{k_{(\text{MB}^*)} I_{\text{MB}}}{I^{(\text{MB}^*)} k_{\text{MB}}} \quad (3)$$

Time-resolved fluorescence spectroscopy (TRFS) is a very good technique to probe the ambient or macromolecule effects on the kinetics as well as dynamics of Photosensitizers [26,27]. Fluorescence lifetime measurements were performed using the time-correlated single photon counting (TCSPC) setup (FL920, Edinburgh Instrument, UK) with 405 nm diode laser and the fluorescence decay was collected at magic angle polarization (55°). The time resolution for TCSPC setup was ~120 ps (measured with LUDOX solution). The emission decay data were analyzed using the software DecayFit-1.4 (for MATLAB®). The fluorescence decay was fitted with sum of three-exponentials to model with the decay pattern given by Eq. (4). The results were fitted best to the triple-exponential fitting function (goodness-of-fit  $\chi^2$ ).

$$\text{Fit} = a_0 + a_1 e^{(-t/\tau_1)} + a_2 e^{(-t/\tau_2)} + a_3 e^{(-t/\tau_3)} \quad (4)$$



where,  $a_0$  is the time shift between IRF (Instrument Response Function) and sample. Their relaxation times are  $\tau_1$ ,  $\tau_2$ , and  $\tau_3$ , and these correspond to various lifetimes of characteristic excited states. For tri-exponential decay law, the average lifetime ( $\tau_{avg.}$ ) was determined by Eq. (5).

$$\tau_{avg.} = a_1 \tau_1 + a_2 \tau_2 + a_3 \tau_3 \quad (5)$$

## 2.6. Bacterial Adherence and Viability Assay

Primary assessments of bacterial adherence after photosensitization of MB and GNP<sub>DEX</sub>-ConA<sub>[MB]</sub> on bacterial cells in microtiter plate as well as on PCTEF (poly-chlorotrifluoroethylene) hydrophobic coverslip (D; 12 mm) (Genetix biotech Asia India) were done by crystal violet adherence reduction assay with slight modifications [28]. The viable of adherent bacteria were performed by XTT viability assay with slight modification as described previously [29]. These methods are briefly described in the Method S8 (Supporting information).

## 2.7. Rate of Singlet Oxygen Generation

The rate of singlet oxygen generation was performed by an indirect method where  $^1O_2$  oxidized the diacetate of dichlorofluorescein (DCFH-DA) to fluorescent form dichlorofluorescein (DCF form) in the bacterial cytoplasm. Here, first of all, bacterial cells incubated with nano-conjugates for 60 min and subsequently a solution of 10 mM DCFH-DA was added and further was incubated for 10, 15, 30 and 60 min in 2 ml well microtiter plate at 37 °C. The cells were photosensitized with laser light. The DCF fluorescence was measured (at  $\lambda_{em} = 522$  nm) following excitation with  $\lambda_{ex} = 490$  nm light. After incubation,  $^1O_2$  production was measured by the amount of fluorescence intensity produced by dichlorofluorescein (DCF) fluorescence (Emission; 520 nm) from bacterial cells as compared to a control cell. Fluorescent intensity of fluorescent probes was measured by Hitachi (Tokyo, Japan) F-4500 × fluorescence spectrometer.

The DCF fluorescence formation can be expressed as Eq. (6) [30], where  $F(t)$  is the intensity of fluorescence at time  $t$ ,  $F_0$  is the fluorescence at initial photosensitization time,  $b$  is a fit parameter, and  $k$  is the time constant, i.e., the inverse of the rate of DCF formation.

$$F(t) = F_0(1 - \beta e^{-(t/k)}) \quad (6)$$

Hence, the rate of DCF formation  $r(t)$  can be calculated from  $d(Ft)/dt$ ; eq. 20.

$$r(t) = \frac{d(Ft)}{dt} = \frac{d}{dt} \left[ F_0 - F_0 \beta e^{-\frac{t}{k}} \right] \quad (7)$$

## 2.8. PCA and Statistical Data Analysis

Principle component analysis was used to reduce the differential correlation data and improve the biasedness of MB, MB@GNP<sub>DEX</sub> and MB@GNP<sub>DEX</sub>-ConA effects in HSA during treatment of bacterial cells. Comprehensive R Archive Network (CRAN) packages (“devtool”, “ggbiplot” and “factextra”) used to PCA [31]. Principal components are calculated as the eigen-vectors of the matrix, yield the variables; cytosolic  $^1O_2$ , ambient  $^1O_2$ , and DAPI fluor. The datasets use to reduce multidimensional information into 2D dataset by  $\log_2$  transformation. The significance and central values of effects (during MB and MB@GNP<sub>DEX</sub>-ConA treatments) were analyzed by open source statistical software R (Comprehensive R Archive Network; CRAN) [31]. Differences between mean values were assessed either by Student's  $t$ -test or by one-way analysis of variance (ANOVA), followed by a Newman-Keuls post-hoc test. Values of  $P > 0.05$  and  $P > 0.001$  were considered to be significant. Non-parametric methods such as Wilcoxon-signed-rank test used as an alternative to paired Student's  $t$ -test and Mann-Whitney- $U$  test used as an alternative to Student's  $t$ -test. Bar

graphs and other plots were prepared by ggplot2 in R. Graph analysis were done by packages (“ggplot2”) downloaded in R console.

## 3. Results and Discussion

### 3.1. Physiochemical and Microscopic Properties

The TEM micrograph of GNP<sub>DEX</sub> clearly showed that dextran forms the stable shell around the GNP<sub>DEX</sub> (approximately  $3 \pm 1.5$  nm, Fig. 1a, inset). Moreover, The FTIR analysis of dextran capped GNP showed C=O stretching vibration of aldehyde group ( $\nu$  1665, Fig. S1a ii, Supporting Information), which may be deduced the reduction of  $Au^{+3}$  to  $Au^0$  by the oxidation of OH into aldehyde groups during the GNP<sub>DEX</sub> formation (Fig. 1a) [22]. The reduction of  $Au^{+3}$  to  $Au^0$  in the colloids is being established by XPS analysis. As shown in figure (Fig. S1 b, Supporting Information), two peaks were observed; the Au 4f<sub>7/2</sub> peak was centered at 83.9 eV and the Au 4f<sub>5/2</sub> peak at 87.3 eV binding energies. The presence of binding energy peaks reveals the conversion of  $Au^{+3}$  to  $Au^0$  [32]. Due to dextran shell coating, GNP<sub>DEX</sub> is incredibly stable at high temperature, extreme pH, and salt concentrations as compared to citrate stabilized GNP [33]. The TEM analysis indicates the uniformity of shape and size of GNP<sub>DEX</sub>, where the majority of nanoparticles have ~23 nm size and have nearly hexagonal symmetry confirmed by x and y-axis shape distribution analysis which is corresponding to surface plasmon resonance (SPR) peak at 533 nm (Fig. 1b, b1 and Fig. S2a, see Supporting Information). The diffraction patterns of XRD (X-ray powder diffraction) and SAED (Selected area electron diffraction) confirmed the face centered cubic (FCC) lattice structure (Fig. S2b, c, Supporting Information). The FCC lattice structure is in concordance with gold crystals at  $2\theta$  values of 38.2° (111), 44.4° (200), 64.6° (220) and 77.5° (311) (JCPDS no. 04-0784) [34] (Method S2, Table S1 and S2, Supporting Information).

The FTIR spectra of MB@GNP<sub>DEX</sub> also support the interaction of MB and GNP<sub>DEX</sub> (Fig. S1a iii, S1a iv, Supporting Information), where the absorption at  $\nu$  1603  $cm^{-1}$  shows the presence of aromatic functionality while absorption peak at  $\nu$  1062 and 1020  $cm^{-1}$  confirmed the presence of C–O and C–N ( $CH_3$ )<sub>2</sub> groups, respectively (Fig. S1a iii, iv, Supporting Information). The C=O absorption peak of GNP<sub>DEX</sub> at  $\nu$  1637.67  $cm^{-1}$  was shifted to the  $\nu$  1665.38  $cm^{-1}$  which revealed its successful conjugation with the MB dye [35]. The  $^1H$  NMR of methylene blue-dextran monomer (i.e. Methyl- $\alpha$ -D-mannopyranoside; a dextran monomer/mannose) complex used to simulate the interactions involved among the MB and GNP<sub>DEX</sub>-ConA. The  $^1H$  NMR of methylene blue-dextran monomer complex showed the presence of the broad multiplet in the range  $\delta$  6.4–6.6 predicted the aromatic signals in the complex. The presence of the four singlets at  $\delta$  1.7–1.9 confirms the presence of the four secondary OH groups (Fig. S1c, Supporting Information). The presence of doublets and quartets in the range of  $\delta$  3.4–4.5 depicted the presence of five CH protons of the D-mannopyranoside ring of the complex. The  $^1H$  NMR of methylene blue-dextran monomer complex confirms the formation of covalently bonded MB-dextran monomer complex, involving OH addition (the 1, 4-addition by the lone pair of electrons of oxygen of  $CH_2$ -OH) of dextran to the  $\alpha$ ,  $\beta$ -unsaturated double bond and later conversion of  $C = N^+(CH_3)_2$  to the  $C-N(CH_3)_2$  (Fig. S1c, Supporting Information).

### 3.2. Optimization of Nano-conjugates

HSA was used as solvent media for MB@GNP<sub>DEX</sub>-ConA, since it is present in infection site/wounds predominantly. This albumin comprises 4.5% protein of total blood plasma protein (7%). It was well known that in vivo condition, antibiotics encounter the HSA and that result in the alteration of in vitro antibiotics properties [36]. Contrary, the cationic photosensitizer is reported to be stable in HSA media and show the significant inhibition of gram-negative and positive bacteria [37]. Herein, the stability of GNP<sub>DEX</sub> (0.25 mg  $ml^{-1}$ ) in HAS (10%) was

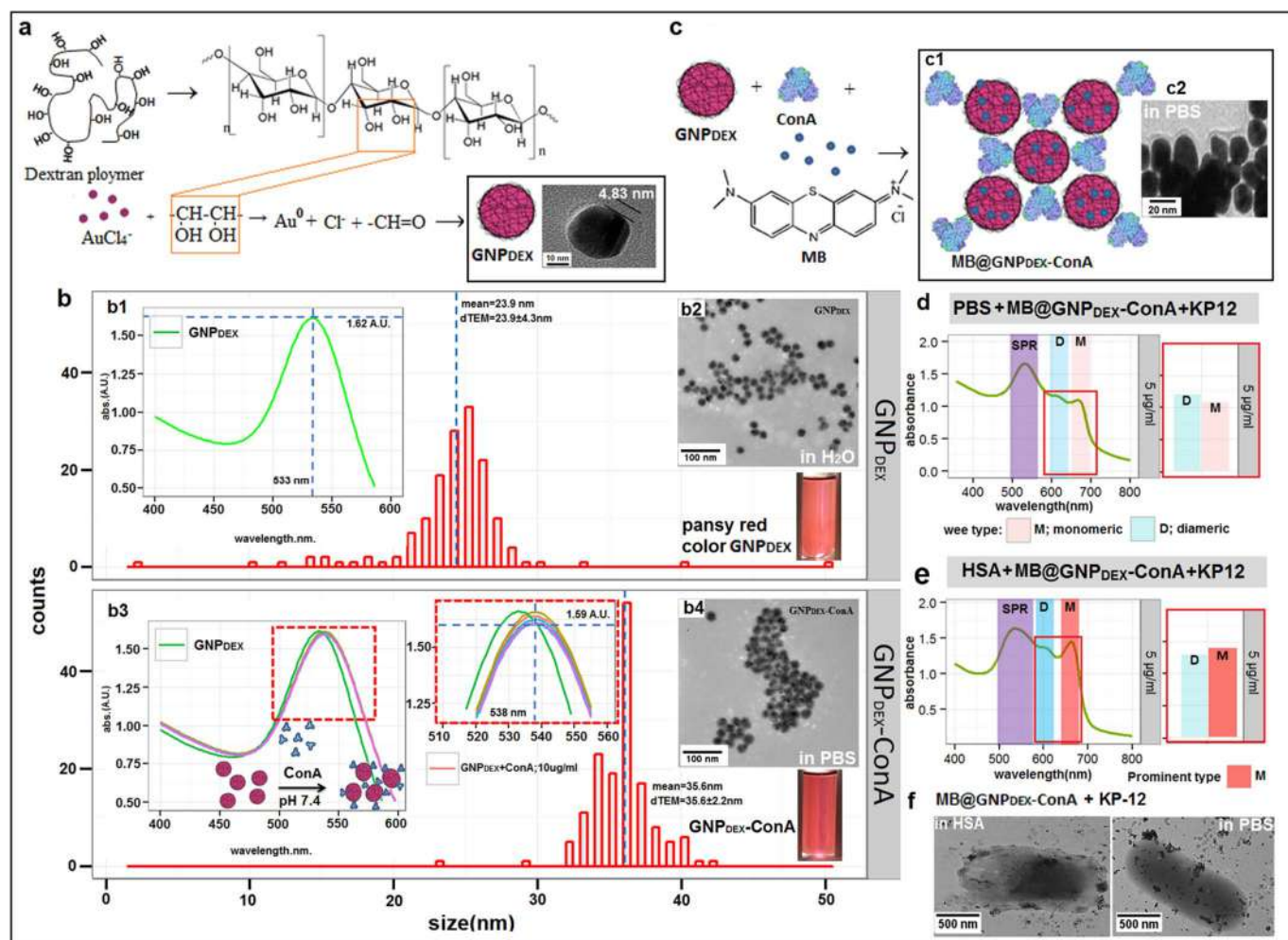


**Fig. 1.** (a) Schematic illustration of dextran capped GNP synthesis. (b) Differential histogram patterns of gold nanoparticles conjugates in HSA (10%) media. (inset; b1) GNP<sub>DEX</sub> (0.25 mg ml<sup>-1</sup>) SPR absorption peak at 533 nm corresponding to pansy red color GNP<sub>DEX</sub> (test tube in inset). (inset; b2) The non-aggregated GNP<sub>DEX</sub> in TEM micrograph. The mean sizes GNP<sub>DEX</sub> are  $23.9 \pm 4.3$  nm and GNP<sub>DEX</sub>-ConA;  $35.6 \pm 2.2$  nm (histogram; by dTEM data analysis in ImageJ; NIH). (inset; b3) Aggregation of GNP<sub>DEX</sub> (0.25 mg ml<sup>-1</sup>) after addition of ConA (5, 10, 15, 20, and 25  $\mu\text{g ml}^{-1}$ ). (c; c1, c2) Schematic illustration of formation of MB@GNP<sub>DEX</sub>-ConA nanoconjugate. (d and e) The SPR, dimeric (D) and monomeric (M) are absorbance peaks of MB@GNP<sub>DEX</sub>-ConA in KP-12 containing media (PBS and HSA). The prominent and wee type absorbance are represented in corresponding bar graphs. (f) The TEM micrograph shows the localization of MB@GNP<sub>DEX</sub>-ConA upon the KP-12 surface in both solvents (HSA and PBS).

analyzed in various pH (7–2) and ionic (NaCl; 1–1000 mM) concentrations. The increased counter-charge concentration around GNP<sub>DEX</sub> got them aggregated, which were distinctly displayed by the flattening of surface plasmon resonance peaks (SPR) (Fig. S4a, S4b, Supporting Information). Remarkably, in presence of HSA (10%), these increased counter-charge concentration diminished, and almost stable SPR peaks depart stability to GNP<sub>DEX</sub> at tested concentrations of NaCl (Fig. S4c, Supporting Information). Further, for optimum photosensitization, nano-conjugates were assessed at different concentration of MB as well as ConA (a mannose specific lectin protein) to derive the efficient working concentrations. After addition of various concentrations of dextran specific ConA (5, 10, 15, 20, and 25  $\mu\text{g ml}^{-1}$ ), UV–vis absorption peak of GNP<sub>DEX</sub> decreased and right shifted, from 533 nm to 538 nm (in control GNP<sub>DEX</sub>; Fig. 1b, b1 to b3 inset). No further shifting of SPR peak was observed after addition of ConA, but beyond the 10  $\mu\text{g ml}^{-1}$  concentration absorption peaks saturated. The aggregation size of GNP<sub>DEX</sub> increased after the addition of 10  $\mu\text{g ml}^{-1}$  ConA to  $35.6 \pm 2.2$  nm (Fig. 1b GNP<sub>DEX</sub>-ConA size histogram) and TEM micrograph also validated the aggregation of GNP<sub>DEX</sub> (Fig. 1b, b4 inset). The ConA (optimum conc. 10  $\mu\text{g ml}^{-1}$ ) aggregated GNP<sub>DEX</sub> were loaded with MB (Fig. 1c), and localized to bacterial surface, where ConA (which have three binding sites for dextrose/mannose) specifically binds to the glucose moiety (i.e. mannose) of lipopolysaccharide

(LPS) of bacterial cell wall [20,22]. Furthermore, absorption spectra of GNP<sub>DEX</sub>-ConA with varying concentration of attached MB (2, 5 and 10  $\mu\text{g ml}^{-1}$ ) were analyzed in presence of KP-12 cells in two ambient solvents (PBS; 7.4pH and HSA; 10%) (Fig. 1d, e, f and Fig. S5, Supporting Information).

Earlier research on the topic has shown the antimicrobial efficacy of nanoparticle-based PDT, but these studies did not consider the involvement of dimeric and monomeric form of photosensitizers in nano-formulation [38]. Herein, we extensively characterized and determined the monomeric MB for the best outcome. The absorption spectra of MB in monomeric and dimeric form showed the different pattern in presence of the nano-conjugates as compared to MB alone (with KP-12 cells in the both media, Fig. S5, Supporting Information). Here, this distribution of total concentration of MB (5  $\mu\text{g ml}^{-1}$ ) in presence of GNP<sub>DEX</sub>-ConA and KP-12 represented as  $C_{\text{total}} = M_{\text{total}} + 2D_{\text{total}}$ , where total concentration of monomeric (M) and dimeric (D) are,  $M_{\text{total}} = M_{\text{free}} + M_{\text{bound}}$  and  $D_{\text{total}} = D_{\text{free}} + D_{\text{bound}}$  and, the x fraction of MB molecules present as monomeric form;  $x = M_{\text{total}} / C_{\text{total}}$ . The equilibrium of dimerization constant of MB ( $M_{\text{total}} \rightleftharpoons 2D_{\text{total}}$ ) is  $K_d = \frac{1-x}{2C_{\text{total}}x^2}$ . The value of the monomeric and dimeric form is the function of the total concentration of MB ( $C_{\text{total}}$ ) [39]. In KP-12 containing HSA solvent media, monomeric MB is prominent at  $C_{\text{total}} = 5 \mu\text{g ml}^{-1}$  and beyond that, the major part of a total

concentration of MB occupied by in dimeric MB form (Fig. 1e, Fig. S5, Supporting Information). Although, the majority of MB at  $5 \mu\text{g ml}^{-1}$  (in HSA) are in monomeric form, but in PBS media both form of MB are in minority or “wee” type (Fig. 1d).

Furthermore, apart from having the zeta potential  $\zeta$ ;  $-3.2 \pm 1.2 \text{ mV}$  and size;  $43.3 \pm 3 \text{ nm}$  (Fig. S6, Supporting Information) in HSA solvent, these MB@GNP<sub>DEX</sub>-ConA attached to KP-12 (Fig. 1f). It is well known that gram-negative bacterial surfaced LPS departs high negative charge or zeta potential ( $\zeta$ ;  $> -20 \text{ mV}$ ) as compared to gram-positive bacterial surface [40,41] and consequently, that will hinder the interaction of MB@GNP<sub>DEX</sub>-ConA ( $\zeta$ ;  $-3.2 \pm 1.2 \text{ mV}$ ) with KP-12. Remarkably, due to the presence of HSA that supposed to counter the same charge repulsion as well as bacterial surface specific ConA leads to interaction among bacterial surface and nano-conjugates. Under antimicrobial perspective, these forms of MB/PS are also responsible for the production of singlet oxygen ( $^1\text{O}_2$ , produced by excited state of monomeric MB/PS) and other free radicals ( $\text{HO}^\bullet$ ,  $\text{H}_2\text{O}_2$  etc., by dimeric MB/PS) [15]. However, bacterial cells have an adequate amount of scavenger such as superoxide dismutase, catalase, and peroxidase to thwarts the free radical (such as  $\text{HO}^\bullet$  and  $\text{H}_2\text{O}_2$ ) mediated bactericidal activity, whereas they have no scavenger against the singlet oxygen molecule and, consequently,  $^1\text{O}_2$  imposed the maximum cell damage [12]. Moreover, singlet oxygen can diffuse to a long distance and even easily cross the cell membrane and stays in the cell for long time [42]. Hence, these  $^1\text{O}_2$  molecules may cause the photo-oxidation of cytoplasmic macromolecules as well as degradation of bacterial DNA.

### 3.3. Monomeric Stages vs. Enhanced Fluorescence Decays

The dimeric and monomeric form ascertained in HSA medium and then correlated with their fluorescence. Illustrative representation of attached MB (monomeric/dimeric) on dextran capped GNP is shown in Fig. 2a. Here, at the lowest concentration, MB exist in mostly

monomeric form but in at highest concentration ( $10 \mu\text{g ml}^{-1}$ ), MB exists in dimeric form predominately (Fig. 2a). Interestingly, the molar extinction coefficient of monomeric MB ( $\epsilon_{\text{max}} = 89,600 \text{ M}^{-1} \text{ cm}^{-1}$ ,  $5 \mu\text{g ml}^{-1}$  MB@GNP<sub>DEX</sub>-ConA in HSA) is higher than MB alone ( $\epsilon_{\text{max}} = 64,000 \text{ M}^{-1} \text{ cm}^{-1}$ ) in same condition (Table S5, Supporting Information). Moreover, after excitation ( $\lambda_{\text{ex}} = 650 \text{ nm}$   $\approx$  to monomeric absorption wavelength), fluorescence emission peak of MB =  $5 \mu\text{g ml}^{-1}$  (MB@GNP<sub>DEX</sub>-ConA) is 1.4 times higher to  $2 \mu\text{g ml}^{-1}$  MB whereas, at MB =  $10 \mu\text{g ml}^{-1}$  fluorescence emission peak drastically decreased (2.3 times) (Fig. 2b, Fig. S7 and Table S6, Supporting Information). There is a strong relation among the emission of fluorescence lifetime and excited state of monomeric MB molecules [26,27]. Analysis of the fluorescence decay kinetics revealed three exponential decays, and corresponding to cumulative/average fluorescence lifetime ( $\tau_f$ ) of MB@GNP<sub>DEX</sub>-ConA in HAS =  $1.7 \text{ ns}$  (Fig. 2c), where this lifetime is the number of excited molecules ( $^3\text{MB}^*$ ) transit to decay to  $1/e$  of the original population. In this transition, MB excited to singlet stage ( $^1\text{MB}^*$ ;  $\text{MB} + h\nu \rightarrow ^1\text{MB}^*$ ) and then intermediate triplet stage  $^3\text{MB}^*$  ( $^1\text{MB}^* \rightarrow ^3\text{MB}^*$ ), and during de-excitation of the  $^3\text{MB}^*$  ( $^3\text{MB}^* \rightarrow \text{MB}$ ), excited stage energy transfer to the surrounding oxygen to produce singlet oxygen ( $^3\text{MB}^* + \text{O}_2 \rightarrow \text{MB} + ^1\text{O}_2$ ) [15]. The cumulative fluorescence decay time of MB alone in HSA is  $0.7 \text{ ns}$  and of MB@GNP<sub>DEX</sub> only is  $1.0 \text{ ns}$  (Table S7, Supporting Information).

### 3.4. Singlet Oxygen Quantification

The  $^1\text{O}_2$  quantum yield was measured by a chemical trapping method with disodium 9, 10-anthracen-dipropionic acid ( $\text{Na}_2\text{-ADPA}$ ,  $^1\text{O}_2$  trapping agent) and MB as the standard photosensitizer ( $^1\text{O}_2$  quantum yield  $\Delta\Phi$ ; 0.52 in water) [43]. First, the light absorbed by MB and MB@GNP<sub>DEX</sub>-ConA calculated by integration of UV-vis light absorbed in the range of 500–700 nm in the form area under the curve AUC (Fig. 3a, b). Second, in the presence of MB@GNP<sub>DEX</sub>-ConA or MB under 660 nm irradiation, the absorbance of the  $\text{Na}_2\text{-ADPA}$  solution at

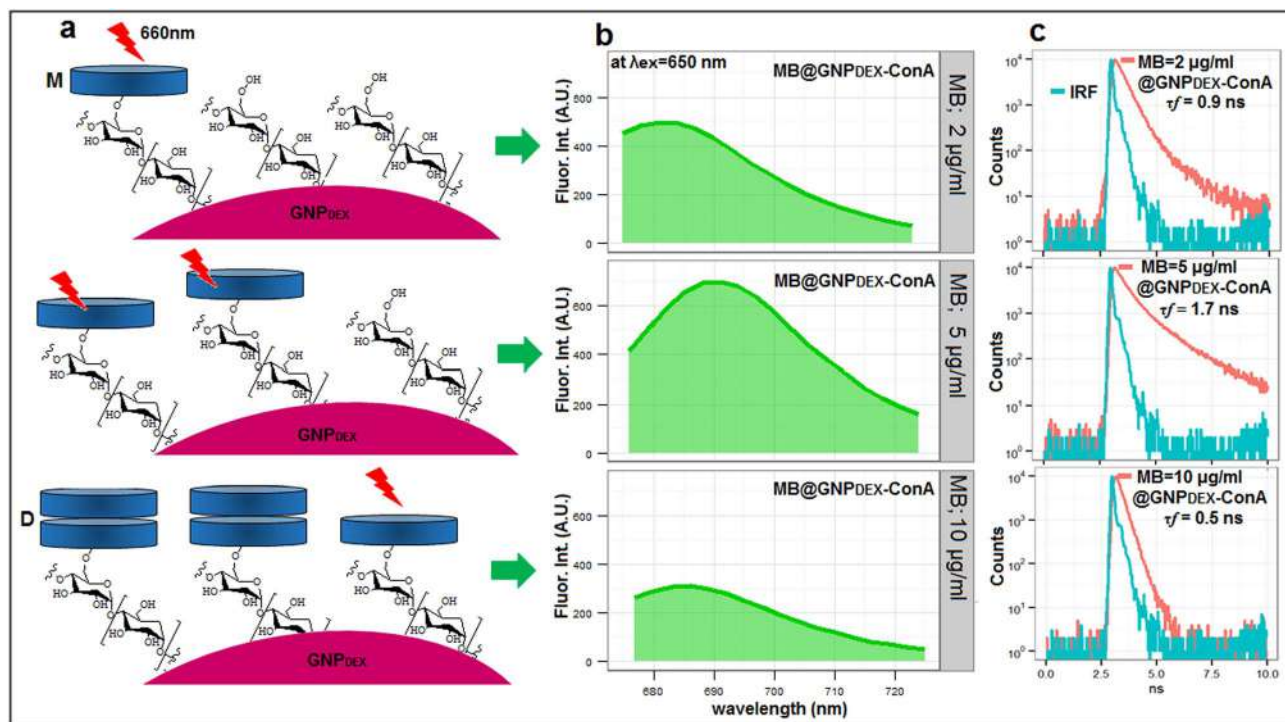


**Fig. 2.** (a) Schematic illustrative representation of MB attachment on dextran capped GNP; at the lowest concentration, MB exist in mostly monomeric (M) form but in at highest concentration (MB;  $10 \mu\text{g ml}^{-1}$ ), MB exists in dimeric (M) form predominately. (b) The fluorescence emission peak ( $\lambda_{\text{ex}} = 650 \text{ nm}$ ) of  $5 \mu\text{g/ml}$  MB@GNP<sub>DEX</sub>-ConA is 1.4 times of  $2 \mu\text{g ml}^{-1}$  MB@GNP<sub>DEX</sub>-ConA and 2.3 times of  $10 \mu\text{g ml}^{-1}$  MB@GNP<sub>DEX</sub>-ConA fluorescence emission peak. (c) The time-resolved fluorescent decay spectra ( $\lambda_{\text{ex}} = 640 \text{ nm}$ ) shows the highest average fluorescence lifetime  $\tau_f = 1.7 \text{ ns}$  of MB@GNP<sub>DEX</sub>-ConA.



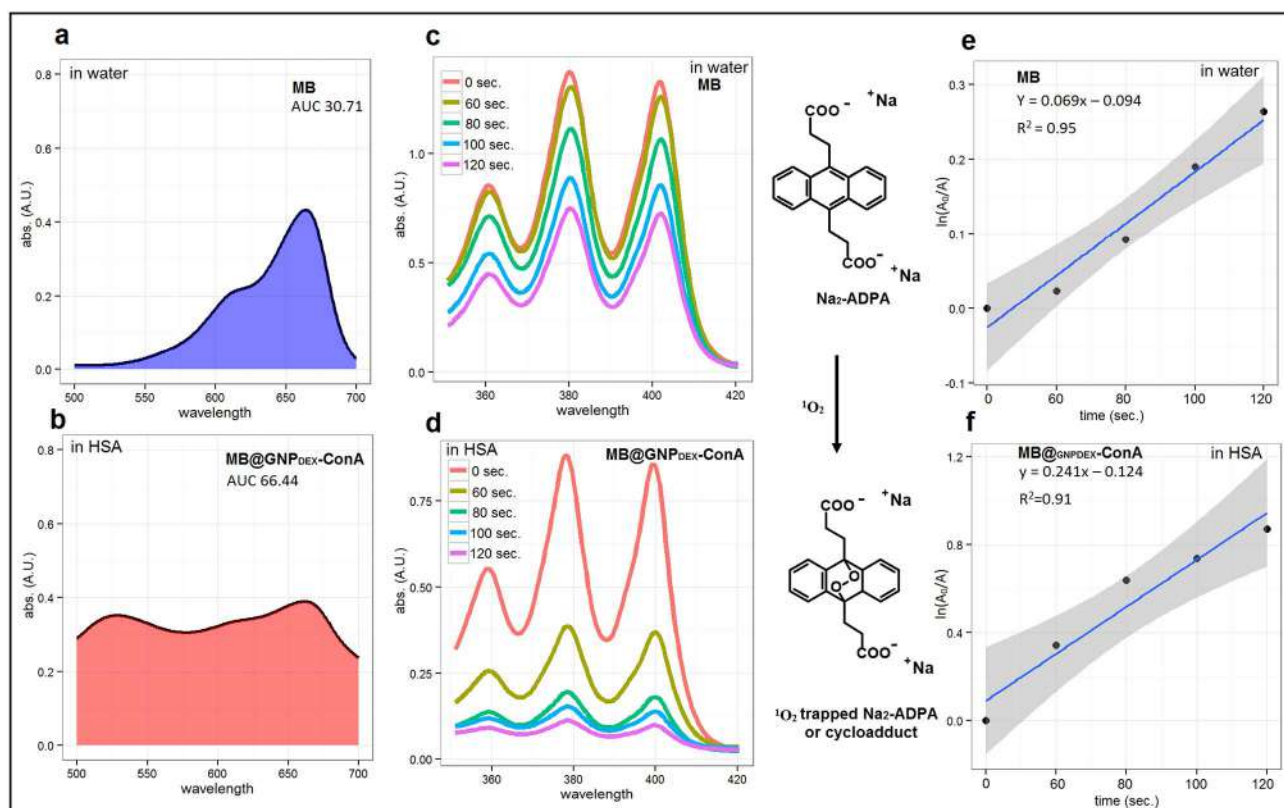


**Fig. 3.** Calculation of singlet oxygen quantum yield. (a and b) The AUC (area under the curve) of UV–vis absorption (MB = 5  $\mu\text{g ml}^{-1}$ ; 30.71 and MB@GNP<sub>DEX</sub>-ConA; 66.44). (c and d) Singlet oxygen trapping by Na<sub>2</sub>-ADPA after irradiation of MB and MB@GNP<sub>DEX</sub>-ConA (irradiation 0–120 s. in water/HSA). The Na<sub>2</sub>-ADPA from the cycloadduct after trapping the <sup>1</sup>O<sub>2</sub> and departs the lowering of UV–vis absorption. (e and f) The calculation of decomposition rate constants of Na<sub>2</sub>-ADPA after the entrapment of <sup>1</sup>O<sub>2</sub> produced by MB and MB@GNP<sub>DEX</sub>-ConA.

378 nm was decreased gradually with prolonged irradiation time, indicated the decomposition of <sup>1</sup>O<sub>2</sub> trapped Na<sub>2</sub>-ADPA (Fig. 3c, d). The plot of relative decomposed ( $\ln[\text{ADPA}]_t/[\text{ADPA}]_0$ , Eq. (2) in [Materials and Methodology](#)) in the form of linear regression line drew the rate constant of decomposition (Fig. 3e, f). The <sup>1</sup>O<sub>2</sub> quantum yield  $\Delta\Phi$  was calculated by the formula (Eq. (3) in [Materials and Methodology](#)). Furthermore, quantum yield also depends upon the dissolved normal oxygen (triplet oxygen; <sup>3</sup>O<sub>2</sub> i.e.  $7.00 \pm 1.8 \text{ mg ml}^{-1}$  in HSA + MB@GNP<sub>DEX</sub>-ConA and  $5.8 \pm 0.7 \text{ mg ml}^{-1}$  in PBS + MB@GNP<sub>DEX</sub>-ConA) (Fig. S8a, S8c and Table S8, Supporting Information). The relative entrapment of produced singlet oxygen (i.e. in HSA, PBS) (Fig. S8d, 14e, Supporting Information) and decomposition constant (i.e.  $k = 63 \times 10^{-2}$  in HSA and  $40 \times 10^{-2}$  PBS; Fig. S9, Supporting Information) also depend upon the dissolved oxygen in given ambient media. Thus, the <sup>1</sup>O<sub>2</sub> quantum yield ( $\Delta\Phi$ ) of the MB@GNP<sub>DEX</sub>-ConA solution was calculated to be 0.84. Moreover, MB@GNP<sub>DEX</sub>-ConA shows the enhanced  $\Delta\Phi$  quantum yield in HSA (10%) medium as compared to H<sub>2</sub>O ( $\Delta\Phi = 0.53$ ), PBS ( $\Delta\Phi = 0.42$  in 7.4 pH), saline ( $\Delta\Phi = 0.50$ , at 0.9% w/v NaCl), MH broth ( $\Delta\Phi = 0.51$ ), and blood plasma ( $\Delta\Phi = 0.64$ ) (Table S8, Supporting Information). Herein, monomeric MB and the availability of dissolved oxygen are responsible for the enhanced singlet quantum yield. Moreover, monomeric MB was attached upon 3–4 nm thick dextran coated GNP<sub>DEX</sub> and it has been reported that spatially arranged MB around GNP (i.e. “closed proximity” of MB) increased the triplet <sup>3</sup>MB\* (two-fold) and rendered the maximum <sup>1</sup>O<sub>2</sub> generation as compared to free as well direct attached MB [18].

### 3.5. Cell Inhibition

It is prerequisite to examine the MB@GNP<sub>DEX</sub>-ConA photostability (i. e. in presence of light only/+L, – cells), dark toxicity (i. e. – L,

+ cells) and light toxicity (+ L, + cells) before the assessment of bacterial inhibition. The photostability showed no obvious decline in absorbance of MB@GNP<sub>DEX</sub>-ConA (continuous treatment 1–7 min.), and degradation of attached MB is lower in HSA media (in HSA, degradation constant:  $k = -0.0173$  ( $R^2$  0.74) >  $k = -0.0184$  ( $R^2$  0.80) in PBS; Table S9, Supporting Information). For dark toxicity, the 12 h growth curves of KP-12 cells (treatment of 2–15  $\mu\text{g ml}^{-1}$  MB@GNP<sub>DEX</sub>-ConA) showed almost same growth patterns (in lag and log phase) as in control (Fig. S10a, Supporting Information). Moreover, the same growth patterns appeared after the treatment of light only (Fig. S10b, 15–120 s/21.4–171.4  $\text{J cm}^{-2}$ , Supporting Information). To depart the maximum bactericidal effects on the MDR bacteria, new methodology and modality were developed where laser light on aggregated bacterial population inflicted the maximum effect. Here, bacterial cells confined to the 3 mm diameter of 7 mm diameter of microtiter wells and an appropriate 3 mm diameter laser light used to cover the maximum area of bacteria growth in a microtiter plate (Fig. 4a; a1). The laser light traveled to 5.5 mm (100  $\mu\text{l}$ ) in solvent media (10% HSA) that comprised the nanoconjugates (Fig. 4a; a2) (see comprehensive dosimetry parameters: Table S4, Supporting Information). Primarily, bacterial-static minimum inhibitory treatment time or minimum inhibitory light density (MITT/MILD) at three different MB concentrations (2, 5, and 10  $\mu\text{g ml}^{-1}$ ) in the presence of GNP<sub>DEX</sub>-ConA were analyzed (Fig. 4b). The subsequent minimum bactericidal treatment time or minimum bactericidal light density (MBTT/MBLD) was calculated by sub-culturing the tested concentrations on MH agar plates (Fig. 4b). MITT of 5  $\mu\text{g ml}^{-1}$  MB on KP-12 are 100 s (142.9  $\text{J cm}^{-2}$  MILD) in presence of GNP<sub>DEX</sub>-ConA, whereas MBTT is 120 s (171.4  $\text{J cm}^{-2}$  MBLD), respectively (Fig. 4b; b2). The comprehensive studies (antibiotics vs. MB@GNP<sub>DEX</sub>-ConA) against other MDR strains are listed in Table 1 where the treatment on MDR bacterial strains showed the almost absolute sensitivity for MB@GNP<sub>DEX</sub>-ConA. The synergism of

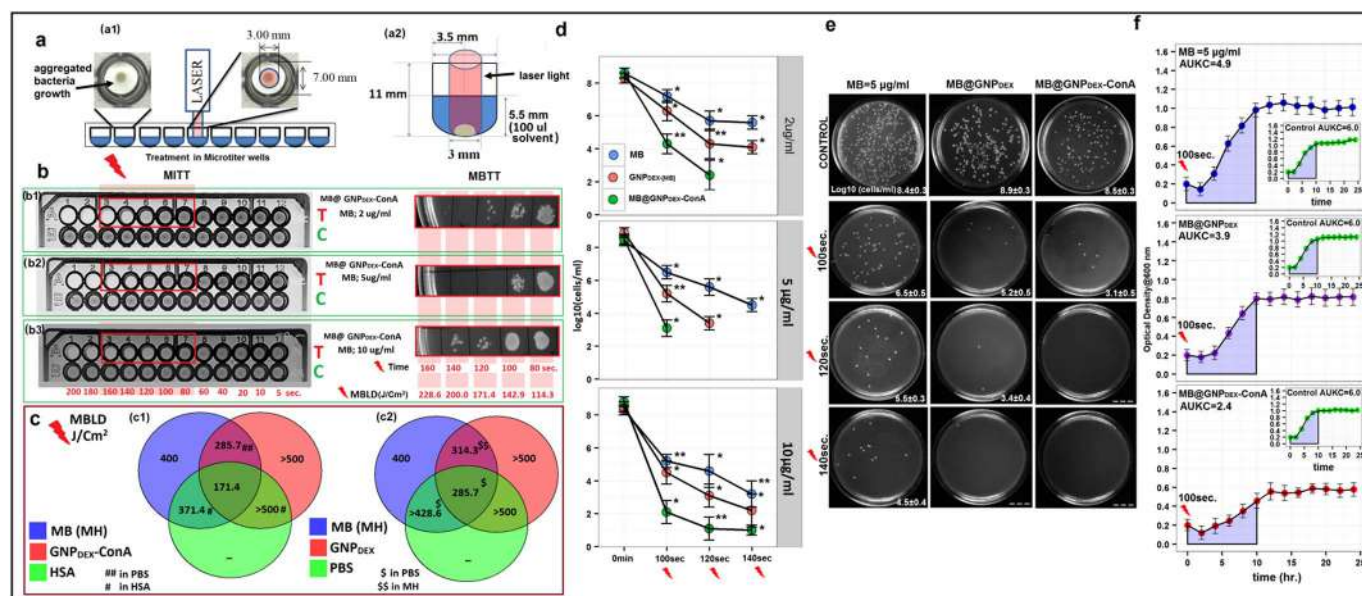


**Fig. 4.** (a; a1 and a2) The methodology and modality of 660 nm laser treatment during calculation of PDT effects in KP-12 containing microtiter plate. (b) The MTT and MBTT of MB@GNPDEX-ConA at different treatments (time in second or MBLD; J/cm<sup>2</sup>) on KP-12. (c) The comparison of MBLD in various combinations of GNPDEX, MB, and GNPDEX-ConA (c1 and c2; combination in HSA and PBS) in the form of Venn diagram. (d) The measurement of viable colony (KP-12 cells) forming units (CFU; log<sub>10</sub> cells ml<sup>-1</sup>) of MB (2, 5, and 10 µg ml<sup>-1</sup>) @GNPDEX and GNPDEX-ConA and (e) viable colonies counts of KP-12 after treatments (at 5 µg ml<sup>-1</sup> MB). (f) The Comparative 24 h bacterial killing curve analysis. The AUKC (area under the killing curve i.e. Initial bacterial growth area covered under the lag and exponential phase) of 5 µg ml<sup>-1</sup> MB@GNPDEX-ConA treatment is 1/2 of control (in inset; without treatment). Error bars indicate the standard error of the mean of three independent experiments performed in triplicates. \* and \*\* represent the significant difference cell viability as compared with control; P > 0.05 and P > 0.001, respectively.

nanoparticles' constituents on KP-12 were analyzed by plotting the MBLD data in Venn diagrams (Fig. 4c). The combination of MB and GNPDEX-ConA in HSA milieu departs the unique enhanced minimum bactericidal light density; MBLD = 171.4 J cm<sup>-2</sup> (Fig. 4c; c1). The MBLD for the same combination in PBS medium was 285.7 J cm<sup>-2</sup>. The nanoparticles, GNPDEX devoid of concanavalinA showed two times higher MBLD (371.4 J cm<sup>-2</sup>) in a combination of MB in PBS (Fig. 4c; c2). The colony forming (CFU) ability of KP-12 (6 × 10<sup>8</sup> cells ml<sup>-1</sup>) was quantified by MB (2, 5, and 10 µg ml<sup>-1</sup>) in presence of GNPDEX-ConA (Fig. 4d). The photosensitization (100 s.) of MB@GNPDEX-ConA

(MB = 5 µg ml<sup>-1</sup>) causes the > 3log<sub>10</sub> reduction in bacterial cells ≈ 97% killing (Fig. 4e). Meanwhile, the log<sub>10</sub> differences during the photosensitization (up to 120 s.) of MB alone (for; 2, 5 and 10 µg ml<sup>-1</sup>) and MB@GNPDEX is not more 3log<sub>10</sub>. The bacterial growth and proliferation ability depends on initial growth rate, hence area covered under the lag and exponential phase was considered as the area under killing curve, AUKC [44]. The AUKC was measured by "MESS" package (downloaded in R console) where the value "spline" results in the area under the natural cubic spline interpolation. The rate of killing is inversely related to the AUKC; i.e. faster the rate of killing, smaller the

**Table 1**

The comparison of antibiotic resistance of clinical isolate bacterial strains against the PDT.

Treatments	<i>Klebsiella pneumoniae</i>					<i>Escherichia coli</i>		<i>Enterobacter cloacae</i>
	KP-12	KP-160	KP-113	KP-229	KP-227	D253	D295	EC-15
antibiotics	AMP	R*	R*	R*	R*	R*	R*	R*
	KAN	R*	R*	R*	R*	R*	R*	R*
	STR	R*	R*	R*	R*	R*	R*	R*
	TET	R*	R*	R*	R*	R*	R*	R*
	AMX	R*	R*	R*	R*	R*	R*	R*
	PIP	R*	R*	R*	R*	R*	R*	R*
	OXA	R*	R*	R*	R*	R*	R*	R*
	CLX	R*	R*	R*	R*	R*	R*	R*
	TIC	R*	R*	R*	R*	R*	R*	R*
	CTX	R*	R*	R*	R*	R*	R*	R*
	CRO	R*	R*	R*	R*	R*	R*	R*
	FOX	R*	R*	R*	R*	R*	R*	R*
PDT <sup>1</sup>	I**	S**	S**	R**	S**	I**	I**	I**
PDT <sup>2</sup>	S**	S**	S**	S**	S**	S**	S**	S**
PDT <sup>3</sup>	S**	S**	S**	S**	S**	S**	S**	S**

AMP: ampicillin, KAN: kanamycin, STR: streptomycin, TET: tetracycline, AMX: amoxicillin, PIP: piperacillin, OXA: oxacillin, CLX: cloxacillin, TIC: ticarcillin, CTX: cefotaxime, CRO: ceftriaxone, FOX: cefoxitin.  
PDT=MB@GNPDEX-ConA, and 1=114.3 J cm<sup>-2</sup>, 2=142.9 J cm<sup>-2</sup>, 3=171.4 J cm<sup>-2</sup>  
R=resistant  
I=intermediate sensitive  
S=sensitive  
Antibiotics concentration breakpoint (for R, I and S) used according to CLSI 2015.  
\* represents the activity tested in Cationic Adjusted Muller Hinton media (CAMH).  
\*\* represents the activity tested in HSA media.



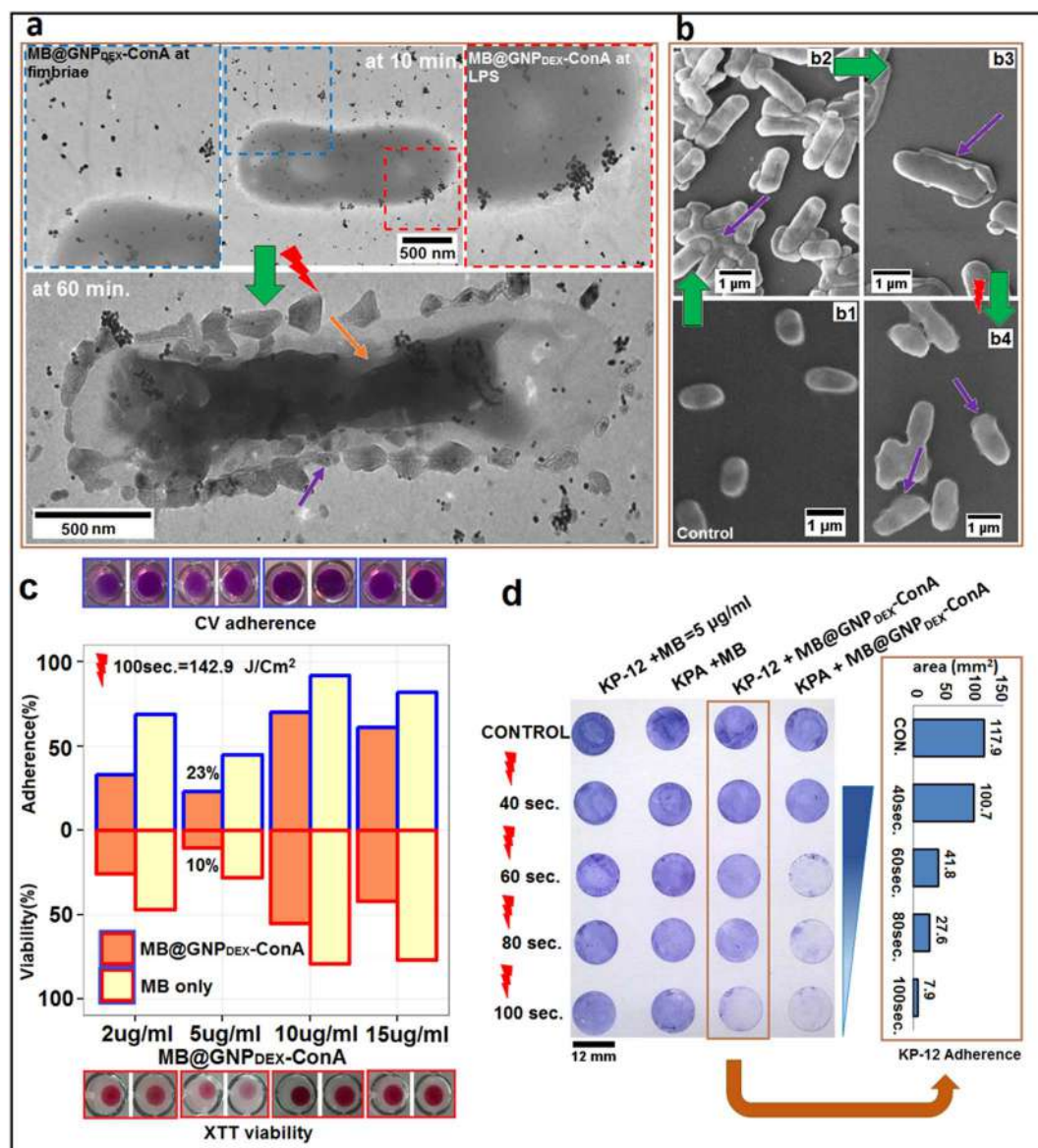


**Fig. 5.** (a) TEM micrographs of localized MB@GNP<sub>DEX</sub>-ConA on KP-12 bacterial surface and treated (for 100 s = 142.9 J cm<sup>-2</sup>) bacterial cell (after 60 min). The micrograph shows the cytological mass with aggregated nanoconjugates (yellow arrow) and cell surface perturbation (violet arrow). (b) The morphological perturbations shown by SEM micrographs. (b; b1) The intact and uniform morphology of control cells and (b; b2 and b3) bacterial aggregation due to ConA mediated attachment of nanoconjugates (violet arrow). (b; b4) The micrograph shows cell membrane destruction (violet arrow) after photosensitization. (c) The proportionality among the % viability (XTT) and adherence (CV) of KP-12 in microtiter plate serial dilution of MB (@GNP<sub>DEX</sub>-ConA). (d) The surface area of adherent (KP-12 and reference bacteria KPA) cells on PCTEF; poly-chlorotrifluoroethylene hydrophobic coverslip after treatment of MB and MB@GNP<sub>DEX</sub>-ConA (MB = 5 μg ml<sup>-1</sup>). (For interpretation of the references to color in this figure legend, the reader is referred to the web version of this article.)

AUKC. The AUKC of MB@GNP<sub>DEX</sub>-ConA (MB = 5 μg ml<sup>-1</sup>), is two times of MB alone (Fig. 4f). For the future in vivo perspective, the viability assay (MTT, method; Method S7, Supporting Information) on HEK293 revealed that 94% cells are viable at the same treatment (photosensitization of 5 μg ml<sup>-1</sup> = MB@GNP<sub>DEX</sub>-ConA) (Supporting Information Fig. S11; a) and further in CLSM micrographs (Supporting Information Fig. S12), the treated HEK293 cells show no cytological perturbation (Comprehensive result in Result S1, Supporting Information).

### 3.6. The Mode of Interactions and Effects

The dual complementary approach used to MB@GNP<sub>DEX</sub>-ConA localization, first; dextran polysaccharide (present on GNP<sub>DEX</sub>, made of mannose monomer) specifically attached to bacterial surfaced fimbriae (FimH; type-I protein) by catch-bond interaction [45]. Second;

Concanavalin-A helped the MB@GNP<sub>DEX</sub> attachment on bacterial surfaced mannose type (monomer of lipopolysaccharide, LPS) [46]. Herein, during early localization (after 10 min incubation), the nanoconjugates initially encounters the bacterial surfaced fimbriae and then bacterial surfaced LPS (Fig. 5a; inset). After the treatment (at 60 min.), bacterial cells surface disintegrated (shown by the violet arrow) and the nanoconjugates are concentrated within the cytoplasmic mass (shown by the yellow arrow) (Fig. 5a). Meanwhile, SEM micrograph showed the aggregation of MB@GNP<sub>DEX</sub>-ConA on the bacterial surface after early localization (at 10 min) and resulted the bacterial cells conglomeration with the help of ConA (Fig. 5b; b2, b3, violet arrows). Interestingly, it was reported that aggregated GNP nanoconjugates also depart the maximum <sup>3</sup>MB\* formation than dispersed nanoconjugates [47]. Hence, after the treatment, SEM micrograph displayed the loss of cell wall integrity (Fig. 5b; b4 violet arrows). The ability of bacterial adherence and viability after treatment were analyzed by Crystal violet



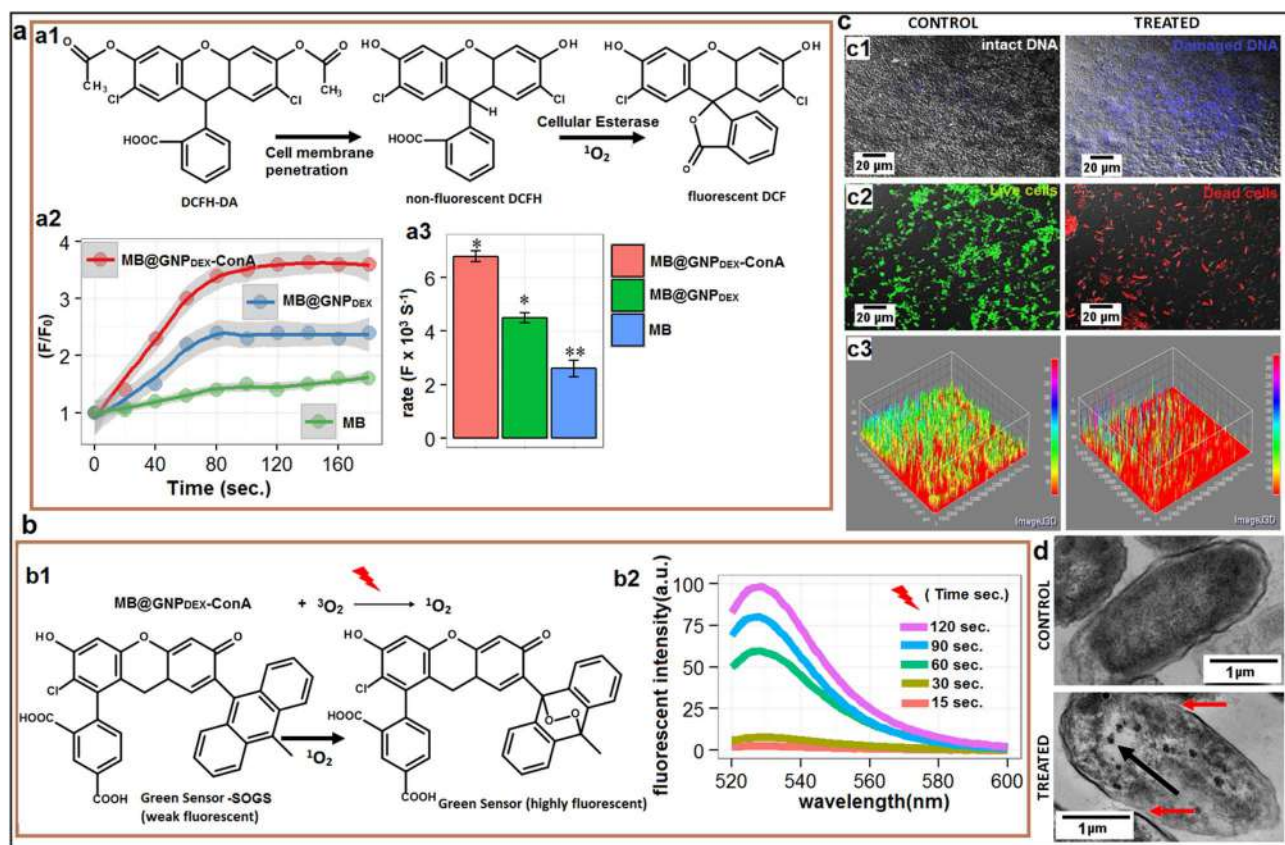


**Fig. 6.** (a) Quantification of ( $^1\text{O}_2$  induced) cytoplasmic DCF green fluor generation (after MB =  $5\ \mu\text{g ml}^{-1}$ , MB@GNP<sub>DEX</sub> and MB@GNP<sub>DEX</sub>-ConA treatment). (a1) The enhancement of the fluorescence ( $F/F_0$  at 0 to 180-second photosensitization) and (a2) the rate of fluorescence ( $F \times 10^{-3}\ \text{s}^{-1}$  at 120-second photosensitization); corresponding to singlet oxygen production. Error bars indicate the standard error of the mean of three independent experiments performed in triplicates. \* and \*\* represent the significant difference in fluorescence intensity as compared with control;  $P > 0.05$  and  $P > 0.001$ , respectively. (b, b1) The singlet oxygen detection probe; SOGS<sup>(R)</sup> for singlet oxygen detection (green fluorescent endoperoxide SOGS formation). (b2) The increment of singlet oxygen generation (SOGS fluorescence intensity at  $\lambda_{\text{em}} = 525\ \text{nm}$ ) up to 120-second MB@GNP<sub>DEX</sub>-ConA photosensitization. (c, c1) The severe DNA damage (probed by DNA-specific blue fluorescent DAPI intercalation), (c2) PI (red; dead cells) and SYTO<sup>®</sup>-9 (green; live cells) fluorescence for viability of KP-12 after the treatment of MB@GNP<sub>DEX</sub>-ConA (for 100 s =  $142.9\ \text{J cm}^{-2}$ ) and (c3) the 3D surface plots of KP-12 microbial cells were made using 3D Viewer plugin in ImageJ. (d) The TEM micrographs show aggregation of MB@GNP<sub>DEX</sub>-ConA (black arrow) and cell membrane damage (red arrow) in treated cells. (For interpretation of the references to color in this figure legend, the reader is referred to the web version of this article.)

(CV, Fig. S13a, Supporting Information) and XTT viability assays (Fig. S13b, Supporting Information). The concluded analysis of these assay shows the positive relationship between them, wherein the treatment (MB =  $5\ \mu\text{g ml}^{-1}$ @GNP<sub>DEX</sub>-ConA,  $100\ \text{s}/142.9\ \text{J cm}^{-2}$ ) reduced the adherence to 23% and viability to 10% (Fig. 5c). In general the attachment of bacteria to the abiotic surfaces (“hydrophobic”) bolstered by cell surface hydrophobicity, bacterial produced fimbriae and extracellular polysaccharide (EPS) [48]. Mostly fimbriae have a high proportion of hydrophobic amino acid residues that responsible for cell surface hydrophobicity involved in hydrophobic interactions (i.e., among the bacterial cell surface and the abiotic surface). It is reported that *Klebsiella* attaches to a hydrophobic surface, where hydrophobic amino acid residues (of fimbriae) are responsible for hydrophobic interactions [49]. Hence, this adherence on hydrophobic abiotic surfaces, such as PCTEF (poly-chlorotrifluoroethylene) visualized by probing attached bacteria with Crystal Violet dye (Fig. 5d). The adherent area of bacteria was quantified by ImageJ software (ImageJ 1.49 v, <http://imagej.nih.gov/ij/download.html>) [50]. The adherent cells surface area (Threshold value of CV blue pixels; in  $\text{mm}^2$ ) of control (KP-12) was about  $112 \pm 0.38\ \text{mm}^2$  and in MB@GNP<sub>DEX</sub>-ConA treated ( $100\ \text{s}/142.9\ \text{J cm}^{-2}$ ) was about  $1.286 \pm 0.27\ \text{mm}^2$  (i.e., 1.14% left). These comprehensive studies are given in bar graphs (Fig. S14, Supporting Information) where given treatment show the same trends even in reference strain KPA. The adherence and viability are proportional to each other and this treatment not only perturbs the outer defense layer (cell wall and cell membrane) but also ultimately kills them.

### 3.7. Cytosolic and Ambient Singlet Oxygen

The DCFH-DA (2', 7'-dichlorodihydrofluorescein) is a non-fluorescent compound that easily penetrates the bacterial cell membrane and converts to DCFH. DCFH-DA oxidation by cytosolic singlet oxygen ( $^1\text{O}_2$ ;  $^1\Delta_g$ ) gives rise to 2', 7'-dichlorofluorescein (DCF), a strong fluorescent molecule [30,51]. Here, the internalized DCFH-DA in the presence of cytosolic  $^1\text{O}_2$  (produced by MB) oxidized to DCF fluorescent compound (Fig. 6a, a1). Comparatively, the fluorescence ( $F$  at  $522\ \text{nm}$ ) in the presence of MB@GNP<sub>DEX</sub> and MB@GNP<sub>DEX</sub>-ConA increased higher than MB alone. The enhanced fluorescence ( $F/F_0$ ) that is tantamount to singlet oxygen formation, increased parabolically up to 80-second photosensitization and became constant after attainment of the plateau (Fig. 6a, a2). The initial fluorescence ( $F/F_0$ ) of MB@GNP<sub>DEX</sub>-ConA up to 80-second photosensitization was highest as compared to MB@GNP<sub>DEX</sub> and MB alone. The rate of fluorescence ( $F \times 10^{-3}\ \text{s}^{-1}$  at 120-second photosensitization)  $\approx$  singlet oxygen production is 4-times higher for MB@GNP<sub>DEX</sub>-ConA as compared to MB alone (Fig. 6a, a3). The singlet oxygen detection probe; SOGS<sup>(R)</sup> was used to quantify the singlet oxygen formation during the photosensitization of MB@GNP<sub>DEX</sub>-ConA. In presence of extracellular/ambient  $^1\text{O}_2$ , the weak fluorescent probe SOGS emits strong green fluorescence ( $\lambda_{\text{ex}} = 504\ \text{nm}$ ,  $\lambda_{\text{em}} = 525\ \text{nm}$ ) [52]. This green fluorescence was generated by endoperoxide formation in SOGS (Fig. 6b, b1). In the Fig. 6b; b2, at increasing photosensitization up to 120 s, fluorescence intensity (at  $525\ \text{nm}$ ) of SOGS increased proportionally. The cellular

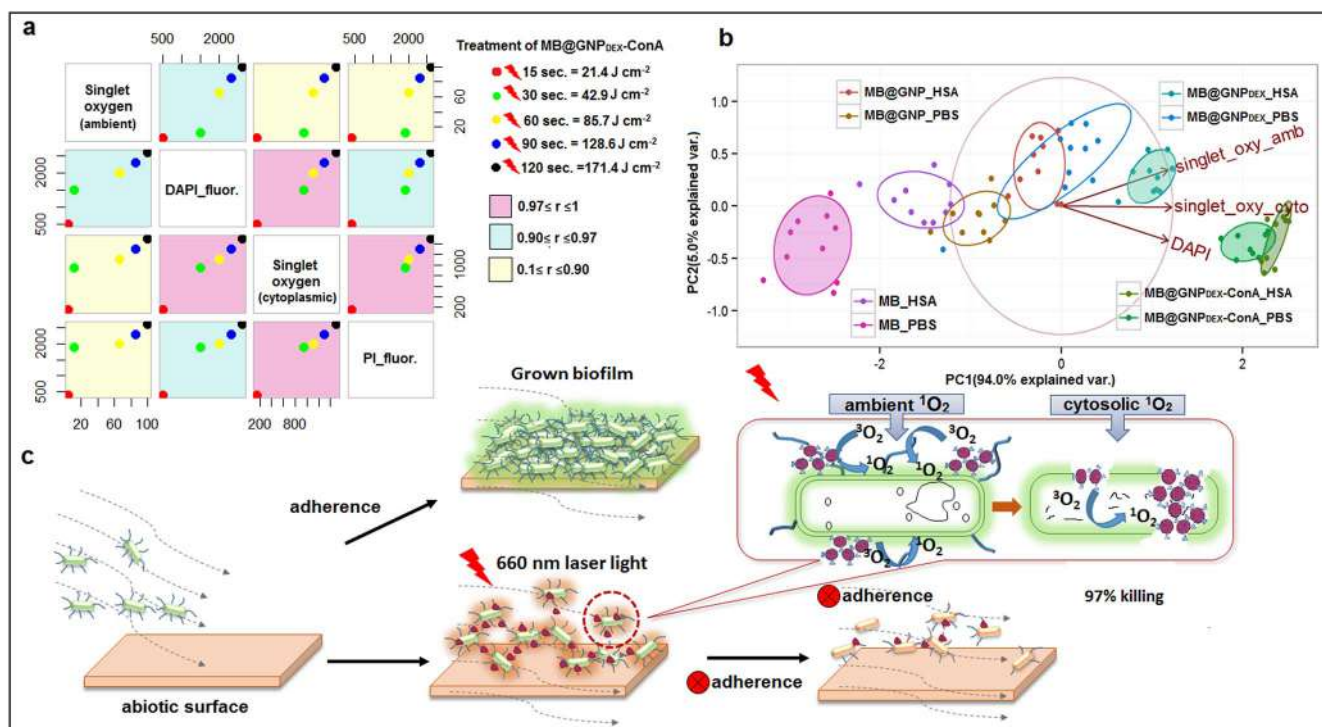


**Fig. 7.** Correlations between singlet oxygen (ambient singlet oxygen; SOGS and cytosolic singlet oxygen; DCFH-DA) and effects (cell death; PI fluor. & DNA degradation; DAPI fluor.) during PDT and their reductive principal component analysis (PCA). (a) The range of correlation coefficient,  $r$  are set at different colors during the treatment of KP-12 at the different successively increasing time period (light density;  $\text{J cm}^{-2}$ ). (b) The biases of different nanoconjugates (at two ambient media; HSA, PBS) toward the cytoplasmic <sup>1</sup>O<sub>2</sub>, ambient <sup>1</sup>O<sub>2</sub>, and nuclear degradation were shown by red arrows. The arrows toward the spindle-shaped distribution of MB@GNP<sub>DEX</sub>-ConA\_HSA attributed to effects (mainly cytoplasmic singlet oxygen mediated nuclear DNA degradation). (c) The illustrative PDT summary; during the photosensitization, the singlet oxygen generates (ambient <sup>1</sup>O<sub>2</sub> and cyto.<sup>1</sup>O<sub>2</sub>), but the bactericidal effect departed by cytosolic singlet oxygen and lack of adherence by ambient oxygen. (For interpretation of the references to color in this figure legend, the reader is referred to the web version of this article.)

target insight of photosensitizer was identified by DAPI; a DNA-specific fluorescent probe (Fig. 6c, c1). The DAPI is planar structured organic molecule that intercalates between DNA base pairs both in both living cells and dead cells [53]. The singlet oxygen destroyed nucleic acids and resulted in severe DNA damage that results in the increased availability of DAPI intercalation; enhanced blue fluorescence ( $\lambda_{\text{ex}} = 350 \text{ nm}$ ,  $\lambda_{\text{em}} = 470 \text{ nm}$ ). In Live-dead cells analysis; PI and SYTO<sup>®</sup>-9 fluorescence probes were used to analysis the viability of KP-12 after the treatment of MB@GNP<sub>DEX</sub>-ConA (Fig. 6c, c2). The SYTO<sup>®</sup> 9 ( $\lambda_{\text{ex}} = 488 \text{ nm}$ ,  $\lambda_{\text{em}} = 498 \text{ nm}$ ) stain generally binds to either intact membranes (i.e., Live cells) or those have damaged membranes. The PI ( $\lambda_{\text{ex}} = 536 \text{ nm}$ ,  $\lambda_{\text{em}} = 617 \text{ nm}$ ) only permeates through the damaged bacterial cell membrane (i.e., Dead cells) and overwhelmed the green fluorescence of SYTO<sup>®</sup> 9 and departs the red fluorescence [54]. CLSM images (Fig. 6c, c2, control and treated) to the 3D surface plot were made using 3D Viewer plugin for ImageJ (Fig. 6c, c3) [55]. Furthermore, the insight of this treatment in bacterial cytosol showed the cell membrane damage and cytoplasmic MB@GNP<sub>DEX</sub>-ConA aggregation (shown by arrow in TEM micrograph; Fig. 6d). The quantification of live and dead cells of KP-12 was done by the basis of CTCF calculations (Method S9, Supporting Information by ImageJ 1.49 v), where the control bar represents the 7.14% cells are dead, and in treated condition 75% cells are dead (Fig. S15, Supporting Information).

### 3.8. Correlations and Principle Component Analysis

The relationship between the singlet oxygen (produced by MB@GNP<sub>DEX</sub>-ConA) and their effects on DNA, as well as viability, were determined by multiple correlation analysis (Fig. 7a). The analytical data was taken in the form of CTCF and fluorescence intensities produced after treatment of the nano-conjugates (photosensitized for 15/21.4, 30/42.9, 60/85.7, 90/128.5 and 120 s/171.4  $\text{J cm}^{-2}$ , Fig. S16,

Supporting Information). There is a positive correlation between the cytosolic singlet oxygen formation and DNA degradation or oxidation ( $0.97 \leq r \leq 1$ ), denoted in the pink color background (Fig. 7a). However, having the same correlation among the bacterial cell death and cytosolic singlet oxygen formation, there is an intermediate correlation between the bacterial cell death and DNA degradation ( $0.90 \leq r \leq 0.97$ , cyan color background, Fig. 7a). Moreover, apart from having the intermediate correlation among the ambient/extracellular oxygen and DNA degradation, there is less correlation among the ambient singlet oxygen vs. cytoplasmic singlet oxygen and bacterial cell death ( $0.1 \leq r \leq 0.90$ , yellow color background, Fig. 7a). Furthermore, Principle component analysis was used to analyze the biasedness (of ambient, cytosolic singlet oxygen and effects; DNA degradation as DAPI fluor.) during photosensitization of nano-conjugates and methylene blue during treatment of KP-12 in various media. Here, in PCA plot the columns (variables; cytosolic <sup>1</sup>O<sub>2</sub>, ambient <sup>1</sup>O<sub>2</sub>, and DAPI fluor.) are arrows and the rows (individuals or treatments; MB\_PBS, MB\_HSA, MB@GNP\_PBS, MB@GNP\_HSA, MB@GNP<sub>DEX</sub>\_PBS, MB@GNP<sub>DEX</sub>\_HSA, MB@GNP<sub>DEX</sub>-ConA\_PBS, and MB@GNP<sub>DEX</sub>-ConA\_HSA) are points or samples (Fig. 7b). Each arrow represents one of the three variables. The first principal component is labeled as PC1 and accounts for almost 94% of the total variation. The first two components (PC1 and 2) explained 99% of the total variance. The eigenvectors indicating an association between variables and PCs are presented in Table S10 (Supporting Information). The bigger the eigen vectors, the higher the correlations between variables and PCs. The variables; cytosolic <sup>1</sup>O<sub>2</sub>, ambient <sup>1</sup>O<sub>2</sub>, and DAPI fluor. were highly positively associated with PC1. The plot of PC1 against PC2 ascertained that points or clusters of (PDT treatments) explained by PC1 that departs the influence by variables (Fig. 7b). The arrow of cytosolic <sup>1</sup>O<sub>2</sub> variable shows its influence upon MB@GNP<sub>DEX</sub>-HSA treatment. However, ambient <sup>1</sup>O<sub>2</sub> and DAPI fluor. variables influence the treatment by photosensitization



of MB@GNP<sub>DEX</sub>-ConA\_PBS and MB@GNP<sub>DEX</sub>-ConA\_HSA.

The produced singlet oxygen involved the killing of bacteria, where it was supposed to depart their effects on bacterial surface and also in the bacterial cytoplasm. Therefore, the cell surface attached nanoconjugates showed the ambient/extracellular singlet oxygen formation (by SOGS green sensor flour, Fig. 6b, b2). And also, the rise of 2', 7'-dichlorofluorescein (DCF fluor.) in bacteria cells further confirmed that cytoplasmic singlet oxygen formation (Fig. 6a, a2). This cytoplasmic singlet oxygen responsible for the nuclear degradation (Fig. 6c, c1) and killing of cells (Fig. 6a, c2). The correlation and consecutive reductive data analysis PCA bolster that cytoplasmic singlet oxygen is a main causative agent for the cells death (Fig. 7a, b). Nevertheless, ambient singlet oxygen around the bacterial cells reduced the adherence capability (Fig. 7c). Apart from that, maybe this singlet oxygen transferred through to bacterial cell wall and cell membrane [42]. Or in another way, destruction of cell wall responsible for impregnations of nanoconjugates responsible for the DNA degradation and eventually cell death during the photosensitization.

#### 4. Conclusion

In summary, we have shown light activated response in MDR clinical strains on treatment with GNP<sub>DEX</sub>-ConA with monomeric forms of MB. We have also shown the plausible mechanism for the singlet oxygen mediated cell membrane damage and cytoplasmic perturbation. With regard to future perspectives, these results showed broad application of this therapy as potential to be translated for the treatment of photo-inactivation in clinical settings, disinfecting surfaces, and other devices. Among the immuno-compromised patients, where MDR biofilm are unsurmountable by the conventional antibiotics, these devised nanoconjugates may be a substitute. It can be applied directly to the localized infection site (which have albumin rich medium), where stabilized monomeric MB may depart effective antibacterial effects. These findings provide an alternative therapeutic option to combat any infections caused by multidrug resistant bacterial strains.

#### Acknowledgements

This work was supported Council of scientific and Industrial Research grant, 37(1576)/13/EMR-II and DST Grant no. SR/NM/NS-41/2016 (G) to AUK. The authors would like to acknowledge Dr. Neetu Singh and Dr. Gajender Saini, Advanced Instrumentation Research Facility, JNU, for providing TRF and HR-TEM instrumental support, respectively. SK thanks CSIR-SRF for the fellowship. We highly appreciate the anonymous reviewers for constructive criticism.

#### Appendix A. Supplementary Data

Supplementary data to this article can be found online at <http://dx.doi.org/10.1016/j.jphotobiol.2017.07.011>.

#### References

- [1] D.L. Paterson, Resistance in gram-negative bacteria: enterobacteriaceae, *Am. J. Med.* 119 (2006) S20–S28 (discussion S62–70).
- [2] S.N. Khan, A.U. Khan, Breaking the spell: combating multidrug resistant 'Superbugs', *Front. Microbiol.* 7 (2016) 174.
- [3] K.K. Kumarasamy, M.A. Toleman, T.R. Walsh, J. Bagaria, F. Butt, R. Balakrishnan, et al., Emergence of a new antibiotic resistance mechanism in India, Pakistan, and the UK: a molecular, biological, and epidemiological study, *Lancet Infect. Dis.* 10 (2010) 597–602.
- [4] R.C. Moellering Jr., NDM-1—a cause for worldwide concern, *N. Engl. J. Med.* 363 (2010) 2377–2379.
- [5] A.U. Khan, P. Nordmann, Spread of carbapenemase NDM-1 producers: the situation in India and what may be proposed, *Scand. J. Infect. Dis.* 44 (2012) 531–535.
- [6] Antibiotic Resistance Threats, CDC, 2013.
- [7] L. Freire-Moran, B. Aronsson, C. Manz, I.C. Gyssens, A.D. So, D.L. Monnet, et al., Critical shortage of new antibiotics in development against multidrug-resistant bacteria - time to react is now, *Drug Resist. Updat.* 14 (2011) 118–124.
- [8] M.R. Hamblin, T. Hasan, Photodynamic therapy: a new antimicrobial approach to infectious disease? *Photochem. Photobiol. Sci.* 3 (2004) 436–450.
- [9] M.A. Biel, L. Pedigo, A. Gibbs, N. Loebel, Photodynamic therapy of antibiotic-resistant biofilms in a maxillary sinus model, *Int. Forum Allergy Rhinol.* 3 (2013) 468–473.
- [10] L. Misba, S. Kulshrestha, A.U. Khan, Antibiofilm action of a toluidine blue O-silver nanoparticle conjugate on *Streptococcus mutans*: a mechanism of type I photodynamic therapy, *Biofouling* 32 (2016) 313–328.
- [11] S. Khan, F. Alam, A. Azam, A.U. Khan, Gold nanoparticles enhance methylene blue-induced photodynamic therapy: a novel therapeutic approach to inhibit *Candida albicans* biofilm, *Int. J. Nanomedicine* 7 (2012) 3245–3257.
- [12] F. Vatansever, W.C. de Melo, P. Avci, D. Vecchio, M. Sadasivam, A. Gupta, et al., Antimicrobial strategies centered around reactive oxygen species—bactericidal antibiotics, photodynamic therapy, and beyond, *FEMS Microbiol. Rev.* 37 (2013) 955–989.
- [13] I.O. Bacellar, T.M. Tsubone, C. Pavani, M.S. Baptista, Photodynamic efficiency: from molecular photochemistry to cell death, *Int. J. Mol. Sci.* 16 (2015) 20523–20559.
- [14] J. Wu, H. Xu, W. Tang, R. Kopelman, M.A. Philbert, C. Xi, Eradication of bacteria in suspension and biofilms using methylene blue-loaded dynamic nanoplateforms, *Antimicrob. Agents Chemother.* 53 (2009) 3042–3048.
- [15] J.P. Tardivo, A. Del Giglio, C.S. de Oliveira, D.S. Gabrielli, H.C. Junqueira, D.B. Tada, et al., Methylene blue in photodynamic therapy: from basic mechanisms to clinical applications, *Photodiagn. Photodyn. Ther.* 2 (2005) 175–191.
- [16] D. Severino, H.C. Junqueira, M. Gugliotti, D.S. Gabrielli, M.S. Baptista, Influence of negatively charged interfaces on the ground and excited state properties of methylene blue, *Photochem. Photobiol.* 77 (2003) 459–468.
- [17] A. Chakraborty, K.D. Held, K.M. Prise, H.L. Liber, R.W. Redmond, Bystander effects induced by diffusing mediators after photodynamic stress, *Radiat. Res.* 172 (2009) 74–81.
- [18] N.L. Pacioni, M. Gonzalez-Bejar, E. Alarcon, K.L. McGilvray, J.C. Scaiano, Surface plasmons control the dynamics of excited triplet states in the presence of gold nanoparticles, *J. Am. Chem. Soc.* 132 (2010) 6298–6299.
- [19] C.C. Huang, C.T. Chen, Y.C. Shiang, Z.H. Lin, H.T. Chang, Synthesis of fluorescent carbohydrate-protected Au nanodots for detection of Concanavalin A and *Escherichia coli*, *Anal. Chem.* 81 (2009) 875–882.
- [20] M.D. Oliveira, C.A. Andrade, M.T. Correia, L.C. Coelho, P.R. Singh, X. Zeng, Impedimetric biosensor based on self-assembled hybrid cysteine-gold nanoparticles and Cramoll lectin for bacterial lipopolysaccharide recognition, *J. Colloid Interface Sci.* 362 (2011) 194–201.
- [21] V. Wittmann, Structural investigation of multivalent carbohydrate-protein interactions using synthetic biomolecules, *Curr. Opin. Chem. Biol.* 17 (2013) 982–989.
- [22] S. Nath, C. Kaitanis, A. Tinkham, J.M. Perez, Dextran-coated gold nanoparticles for the assessment of antimicrobial susceptibility, *Anal. Chem.* 80 (2008) 1033–1038.
- [23] A.U. Khan, P. Nordmann, NDM-1-producing *Enterobacter cloacae* and *Klebsiella pneumoniae* from diabetic foot ulcers in India, *J. Med. Microbiol.* 61 (2012) 454–456.
- [24] W. Tang, H. Xu, R. Kopelman, M.A. Philbert, Photodynamic characterization and in vitro application of methylene blue-containing nanoparticle platforms, *Photochem. Photobiol.* 81 (2005) 242–249.
- [25] M. Hoebeke, X. Damoiseau, Determination of the singlet oxygen quantum yield of bacteriochlorin a: a comparative study in phosphate buffer and aqueous dispersion of dimiristoyl- $\alpha$ -phosphatidylcholine liposomes, *Photochem. Photobiol. Sci.* 1 (2002) 283–287.
- [26] H. Schneckenburger, H.K. Seidlitz, J. Eberz, Time-resolved fluorescence in photobiology, *J. Photochem. Photobiol. B* 2 (1988) 1–19.
- [27] S.-C.A. Yeh, M.S. Patterson, J.E. Hayward, Q. Fang, Time-resolved fluorescence in photodynamic therapy, *Photonics, Multidisciplinary Digital Publishing Institute*, 2014, pp. 530–564.
- [28] J.H. Merritt, D.E. Kadouri, G.A. O'Toole, Growing and analyzing static biofilms, *Curr. Protoc. Microbiol.* 1B (2005) 18.
- [29] M.G. Stevens, S.C. Olsen, Comparative analysis of using MTT and XTT in colorimetric assays for quantitating bovine neutrophil bactericidal activity, *J. Immunol. Methods* 157 (1993) 225–231.
- [30] N.A. Daghananli, R. Itri, M.S. Baptista, Singlet oxygen reacts with 2', 7'-dichlorodihydrofluorescein and contributes to the formation of 2', 7'-dichlorofluorescein, *Photochem. Photobiol.* 84 (2008) 1238–1243.
- [31] R.C. Team, R: A Language and Environment for Statistical Computing, (2013).
- [32] A. Kumar, S. Mandal, P. Selvakannan, R. Pasricha, A. Mandale, M. Sastry, Investigation into the interaction between surface-bound alkylamines and gold nanoparticles, *Langmuir* 19 (2003) 6277–6282.
- [33] H. Jang, Y.K. Kim, S.R. Ryoo, M.H. Kim, D.H. Min, Facile synthesis of robust and biocompatible gold nanoparticles, *Chem. Commun.* 46 (2010) 583–585.
- [34] D. Philip, Green synthesis of gold and silver nanoparticles using *Hibiscus rosa-sinensis*, *Phys. E* 42 (2010) 1417–1424.
- [35] E.-K. Lim, E. Jang, J. Kim, T. Lee, E. Kim, H.S. Park, et al., Self-fabricated dextran-coated gold nanoparticles using pyrenyl dextran as a reducible stabilizer and their application as CT imaging agents for atherosclerosis, *J. Mater. Chem.* 22 (2012) 17518–17524.
- [36] S. Schmidt, K. Rock, M. Sahre, O. Burkhardt, M. Brunner, M.T. Lobmeyer, et al., Effect of protein binding on the pharmacological activity of highly bound antibiotics, *Antimicrob. Agents Chemother.* 52 (2008) 3994–4000.
- [37] S.A. Lambrechts, M.C. Aalders, F.D. Verbaak, J.W. Lagerberg, J.B. Dankert, J.J. Schuitemaker, Effect of albumin on the photodynamic inactivation of microorganisms by a cationic porphyrin, *J. Photochem. Photobiol. B* 79 (2005) 51–57.
- [38] S. Perni, P. Prokopovich, J. Pratten, I.P. Parkin, M. Wilson, Nanoparticles: their



- potential use in antibacterial photodynamic therapy, *Photochem. Photobiol. Sci.* 10 (2011) 712–720.
- [39] K. Patil, R. Pawar, P. Talap, Self-aggregation of methylene blue in aqueous medium and aqueous solutions of Bu<sub>4</sub>NBr and urea, *Phys. Chem. Chem. Phys.* 2 (2000) 4313–4317.
- [40] C.S. Alves, M.N. Melo, H.G. Franquelim, R. Ferre, M. Planas, L. Feliu, et al., *Escherichia coli* cell surface perturbation and disruption induced by antimicrobial peptides BP100 and pepR, *J. Biol. Chem.* 285 (2010) 27536–27544.
- [41] T. Velkov, Z.Z. Deris, J.X. Huang, M.A. Azad, M. Butler, S. Sivanesan, et al., Surface changes and polymyxin interactions with a resistant strain of *Klebsiella pneumoniae*, *Innate Immun.* 20 (2014) 350–363.
- [42] E. Skovsen, J.W. Snyder, J.D. Lambert, P.R. Ogilby, Lifetime and diffusion of singlet oxygen in a cell, *J. Phys. Chem. B* 109 (2005) 8570–8573.
- [43] M.C. DeRosa, R.J. Crutchley, Photosensitized singlet oxygen and its applications, *Coord. Chem. Rev.* 233 (2002) 351–371.
- [44] J. Tisdale, M. Pasko, J. Mylotte, Antipseudomonal activity of simulated infusions of gentamicin alone or with piperacillin assessed by serum bactericidal rate and area under the killing curve, *Antimicrob. Agents Chemother.* 33 (1989) 1500–1505.
- [45] M. Forero, W.E. Thomas, C. Bland, L.M. Nilsson, E.V. Sokurenko, V. Vogel, A catch-bond based nanoadhesive sensitive to shear stress, *Nano Lett.* 4 (2004) 1593–1597.
- [46] S. Campuzano, J. Orozco, D. Kagan, M. Guix, W. Gao, S. Sattayasamitsathit, et al., Bacterial isolation by lectin-modified microengines, *Nano Lett.* 12 (2011) 396–401.
- [47] Y. Yang, Y. Hu, H. Du, H. Wang, Intracellular gold nanoparticle aggregation and their potential applications in photodynamic therapy, *Chem. Commun.* 50 (2014) 7287–7290.
- [48] R.M. Donlan, Biofilms: microbial life on surfaces, *Emerg. Infect. Dis.* 8 (2002).
- [49] P. Di Martino, N. Cafferini, B. Joly, A. Darfeuille-Michaud, *Klebsiella pneumoniae* type 3 pili facilitate adherence and biofilm formation on abiotic surfaces, *Res. Microbiol.* 154 (2003) 9–16.
- [50] C.A. Schneider, W.S. Rasband, K.W. Eliceiri, NIH image to ImageJ: 25 years of image analysis, *Nat. Methods* 9 (2012) 671–675.
- [51] N. Soh, Recent advances in fluorescent probes for the detection of reactive oxygen species, *Anal. Bioanal. Chem.* 386 (2006) 532–543.
- [52] X. Ragàs, A. Jiménez-Banzo, D. Sánchez-García, X. Batllori, S. Nonell, Singlet oxygen photosensitisation by the fluorescent probe Singlet Oxygen Sensor Green®, *Chem. Commun.* (2009) 2920–2922.
- [53] J. Kapuscinski, DAPI: a DNA-specific fluorescent probe, *Biotech. Histochem.* (2009).
- [54] P. Stiefel, S. Schmidt-Emrich, K. Maniura-Weber, Q. Ren, Critical aspects of using bacterial cell viability assays with the fluorophores SYTO9 and propidium iodide, *BMC Microbiol.* 15 (2015) 1.
- [55] B. Schmid, J. Schindelin, A. Cardona, M. Longair, M. Heisenberg, A high-level 3D visualization API for Java and ImageJ, *BMC Bioinforma.* 11 (2010) 1.